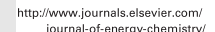


Contents lists available at ScienceDirect

Journal of Energy Chemistry



journal homepage: www.elsevier.com/locate/jechem

Recent progress in solution assembly of 2D materials for wearable energy storage applications

Dong Zhou a,b,1, Liang Zhao a,b,1, Bo Li a,b,*

ARTICLE INFO

Article history: Received 5 October 2020 Revised 20 February 2021 Accepted 1 March 2021 Available online 13 March 2021

Keywords: 2D materials Solution assembly Wearable Energy storage

ABSTRACT

Wearable energy storage devices are desirable to boost the rapid development of flexible and stretchable electronics. Two-dimensional (2D) materials, e.g., graphene, transition metal dichalcogenides and oxides, and MXenes, have attracted intensive attention for flexible energy storage applications because of their ultrathin 2D structures, high surface-to-volume ratio, and unique physical/chemical properties. To achieve commercialization of 2D material-based wearable energy storage devices (2DM-WESDs), scalable and cost-efficient manufacturing is a critical challenge. Among existing manufacturing technologies, solution-based assembly strategies show strong potential to achieve low-cost and scalable production. A timely review of the recent progress in solution-based assembly strategies and the resultant 2DM-WESDs will be meaningful to guide the future development of 2DM-WESDs. In this review, first, a brief introduction of exfoliation and solution preparation of 2D material species from bulk materials is discussed. Then, the solution-based assembly strategies are summarized, and the advantages and disadvantages of each method are compared. After that, two major categories of 2DM-WESDs, supercapacitor and battery, are discussed, emphasizing their state-of-the-art energy storage performances and flexibilities. Finally, insights and perspectives on current challenges and future opportunities regarding the solution assembly of 2DM-WESDs are discussed.

© 2021 Science Press and Dalian Institute of Chemical Physics, Chinese Academy of Sciences. Published by ELSEVIER B.V. and Science Press. All rights reserved.

1. Introduction

Wearable devices currently impact fields as diverse as healthcare, electronics, and personal entertainment with widely used devices ranging from cell phone screens, health trackers to batteries [1–8]. A dedicated integrated wearable electronics system requires all related parts, including the sensing units, antenna, wires, and energy storage system, to be flexible, *i.e.*, bendable and stretchable, to achieve conformal contact with the biointerface during the applications [9,10]. Wearable energy storage is a crucial piece of the integrated wearable electronics system. Higher energy storage capability, higher bendability/stretchability, thinner devices, and larger-scale and lower-cost manufacturing are the inherent driving forces of technical innovations in the field [11,12]. Two-dimensional (2D) materials are believed to be innovative and promising candidates for future wearable energy storage applications due to the thin 2D geometry and excellent electrical, electrochemical, and mechanical properties [13–19]. First, the atomic-scale thickness with excellent mechanical properties confers flexibility and durability [20,21]. Second, 2D nanosheets present ultra-large specific surface area and excessive edges with exposed atoms for charge storage and transfer, and catalytic processes [22,23]. Third, the 2D material is a vast collection of materials with various chemical compositions and adjustable electrical and electrochemical properties [24–28].

The development and commercialization of 2D materials-based wearable energy storage devices (2DM-WESDs) are in the early stages, although a significant amount of progress has been made. There are several substantial objectives to achieve: high manufacturing scalability and reproducibility, affordable cost, high device performances, and high flexibility. From the manufacturing point of view, there are two major steps: (1) preparing the raw materials into high-quality 2D nanosheets and (2) integrate 2D nanosheets onto flexible substrates (e.g., polymer films and metal foils) as electrodes for energy storage devices. To date, the liquid phase-based exfoliation from bulk layered materials has the lowest cost, most massive productivity, and highest scalability [29]. Moreover, the

^a Department of Mechanical Engineering, Villanova University, Villanova, PA 19085, USA

^b Hybrid Nano-Architectures and Advanced Manufacturing Laboratory, Villanova University, Villanova, PA 19085, USA

^{*} Corresponding author at: Department of Mechanical Engineering, Villanova University, Villanova, PA 19085, USA.

E-mail address: bo.li@villanova.edu (B. Li).

¹ These authors contributed equally to this work.

solution assembly technologies show promise in manufacturing wearable energy devices on a large scale [30]. It is crucial to provide a timely review of recent progress in solution assembly of 2D materials for wearable energy storage devices and highlight the challenges to address and opportunities to embrace. As shown in Fig. 1, we will first introduce the preparation of 2D nanosheets using scalable exfoliation methods, and then summarize solution assembly strategies that can be or have been used to prepare flexible/stretchable electrodes for wearable supercapacitors and batteries. Further, the state-of-the-art performance of 2D materialbased wearable supercapacitors and batteries obtained using assembly methods will be compared with a particular emphasis on flexible stability, i.e., device performance under bending and stretching. Finally, the challenges of 2DM-WESDs obtained from solution-based assembly strategies will be analyzed, and an outlook for future opportunities will be provided. To provide a most up-to-date review, we will only summarize the progress of wearable supercapacitors and batteries in the recent five years.

2. Preparation of two-dimensional nanosheet solutions

The solution-based assembly strategies using 2D nanosheet solutions represent the most viable route of transforming the application of 2D materials from lab scale to industrial scale. This is because of the encouraging progress in achieving a costeffective and large-scale 2D nanosheet solution [31]. Generally, the 2D nanosheet solution preparation strategies can be classified into bottom-up and top-down strategies. The bottom-up strategies synthesize 2D nanosheets through a controlled wet chemical reaction (e.g., electrochemical deposition), which achieves anisotropic growth of sheets with atomic thickness [32]. The top-down strategies delaminate or exfoliate 2D nanosheets from the bulk crystals of layered materials [33]. The top-down strategies are prevailing in the solution-based assembly methods because of their largescale productivity and low manufacturing cost. In this section, we will focus on top-down strategies, i.e., micromechanical cleavage, chemical reaction assisted exfoliation, and exchange strategies, reviewing their core principles and procedures.

2.1. Micromechanical cleavage

Since the successful isolation of monolayer graphene using scotch tape in 2004 [34], the exfoliation of bulk layered materials into monolayer 2D nanosheets in the solvent has been widely explored and extended. The principle utilizes the mechanical force to break down the interaction between the layers and separate the 2D nanosheets under the liquid environment. Typically, ultrasonication and ball milling have been adopted to generate micromechanical cleavage forces, though the controlling mechanisms are different. Sonication creates bubbles in the solvents, and the collapse of these bubbles will generate ultrahigh temperature, pressure, and high velocity and thus break the interlayer interaction [35]. Coleman and his co-workers first demonstrated the exfoliation of graphite using sonication in 2008 [36]. In the past decade, many 2D materials (e.g., graphene, MoS₂, h-BN, and NbSe₂) have been exfoliated successfully using sonication, and the controlling factors have been studied and summarized systematically (Fig. 2a) [37]. For example, Liu et al. reported MoS₂/graphene mixture using ultrasonic assisted exfoliation, which achieves high capacity and excellent cycle stability for Lithium ion batteries (LIBs) (Fig. 2b) [38]. The exfoliation efficiency depends on several important parameters, such as the solvent, stabilizer, energy input (sono energy), and treatment time. These factors are coupled together leading to difficulties in controlling the exfoliation process and thereafter a wide size distribution, *i.e.*, lateral dimension and layer thickness, of the 2D nanosheet.

Ball milling utilizes high shear force to delaminate layered materials, and it can also generate 2D nanosheets in large quantities. The milling device usually contains a rotatable chamber with metal or ceramic balls inside. When rotating the chamber, the collisions among the balls and between balls and the wall of the chamber create a strong shear force for the delamination. Under the effect of shear, the slip between layers in the in-plane direction can achieve isolated few-layer or monolayer nanosheet [39]. For example, Zhang et al. developed an intermediate-assisted grinding method to exfoliate bulk h-BN into 2D h-BN nanosheets with large flake sizes, high quality, and structural integrity (Fig. 2c) [40]. Modification of the geometry can improve exfoliation quality and efficiency. Yousef et al. replaced the spherical balls with an involuteshaped gear. This design can provide uniform shear, and obtain 91% exfoliation efficiency for graphene nanosheets with an average thickness of 15 nm in dimethylformamide (DMF) for 45 min at the speed of 500 rpm [41]. Although the discussion here focuses on the two most fundamental micromechanical cleavage principles, it is important to note that the combination and transformation of these principles have further led to new technologies such as rotor-stator mixer and kitchen mixer [42,43], mixed sonication and shear [38], grinding-assisted sonication [44], jet cavitation [45], and wet-jet milling [46].

2.2. Chemical reaction assisted exfoliation

The chemical reaction assisted exfoliation is a more efficient but corrosive way to exfoliated or delaminate the bulk layered materials through well-designed chemical reactions (Fig. 3a). One representative example is Hummers' method to exfoliate graphite to graphene oxide (GO) [47,48]. Under the effect of strong oxidative agents, e.g., potassium permanganate concentrated sulfuric acid and nitric acid, the oxidation process of graphite will generate oxygen-containing functional groups and expand the interlayer distance (Fig. 3b) [49]. These hydrophilic functional groups not only significantly decrease interlayer interaction but also facilitate water penetration. Therefore, a mild shear or stirring after the oxidization can exfoliate the GO into nanosheets. However, the oxidization process will damage the intrinsic atomic structure and electrical and mechanical properties of graphene [50]. Thus, reduction procedures are widely adopted to recover GO to reduced GO (rGO) in which the pristine structure and properties of graphene can be partially recovered to meet the conductivity requirement of high-performance supercapacitors and batteries [51,52].

Another widely studied chemical reaction assisted mechanism is the insertion of alkali metals into the layers because of the small size and strong reductive activity of alkali metal atoms or ions. The hydrogen bubbles generated by the reaction between the alkali metals and water can expand the layer distance and achieve the delamination (Fig. 3c). This intercalation of alkali metal atoms into the layers of bulk layered materials needs to be delicately controlled and should be done under a strictly-controlled inert atmosphere because of the high reductive activity of alkali metal atoms. Serials of 2D materials have been exfoliated utilizing this method, such as graphite, hexagonal boron nitride (h-BN), and transition metal dichalcogenides (TMDCs) [53-55]. Currently, this mechanism is not suitable for the exfoliation of layered oxides, e.g., metal oxides, metal hydroxides, and metal-organic frameworks (MOFs) because the alkali metal intercalated layer materials and the resulting solutions are strongly reductive, which may quickly dissolve or degrade the oxides [31].

For MAX phase exfoliation, to diminish the strong interlayer metallic bonding, the etching assisted exfoliation process is widely adopted [56]. The ceramic MAX phase materials usually have a



Fig. 1. Schematic of the main focuses of this review, including the exfoliation of layered materials into 2D nanosheets, their assembly on flexible 1D fibers, 2D planar substrates, or 3D foams/scaffolds, and their integrations into wearable devices for energy storage.

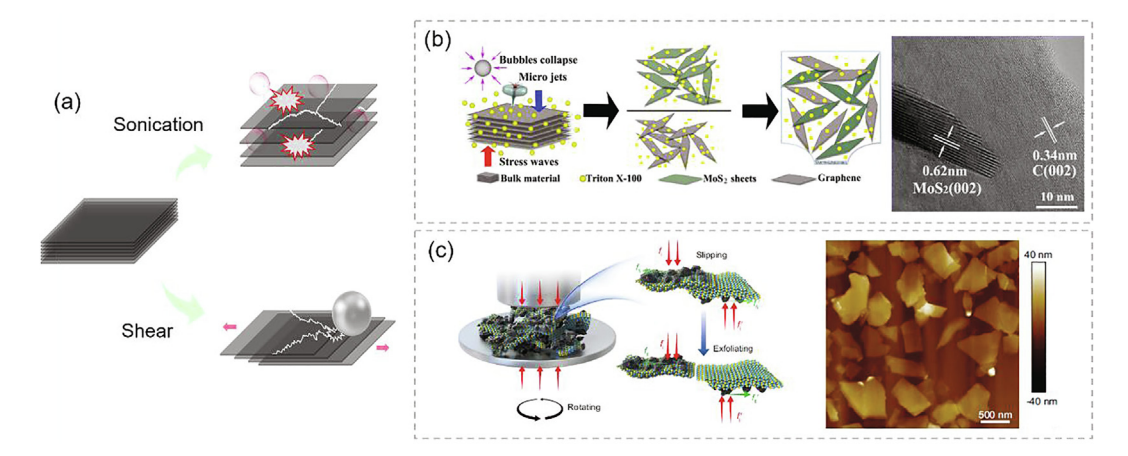


Fig. 2. Micromechanical cleavage strategies. (a) Schematic of micromechanical cleavage exfoliation of 2D materials. (b) Typical processes of ultrasonic assisted exfoliation [38]. (c) Exfoliation mechanism of layer materials and AFM image, statistical analysis of the lateral size and thickness of 2D h-BN nanosheets [40].

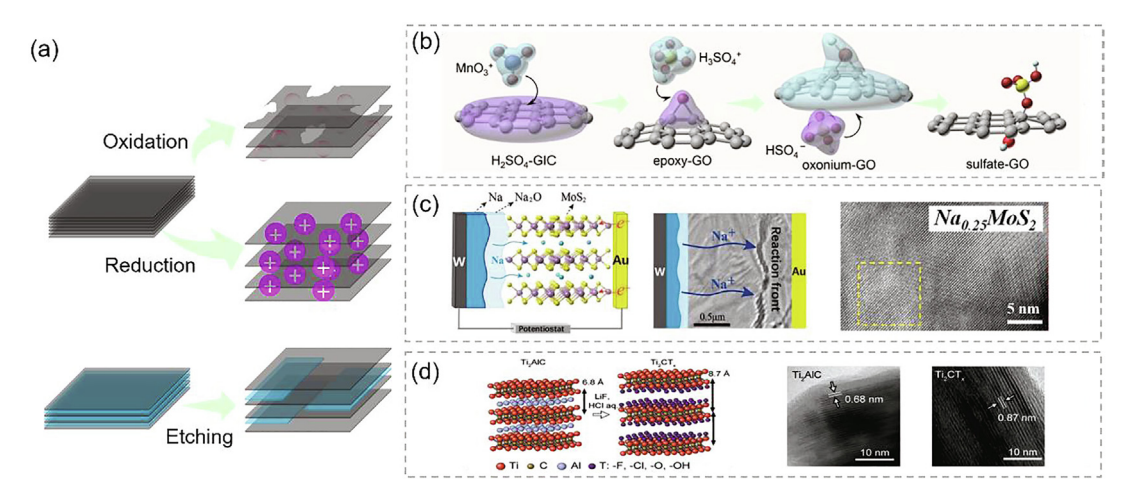


Fig. 3. Chemical reaction assisted exfoliation of 2D materials. (a) Schematics of different chemical paths for exfoliation. (b) Schematic illustration of the intrinsic formation and conversion path of oxygen-containing functional groups on oxidized graphite [49]. (c) Schematic of intercalation process of MoS₂ by metallic Na coated with Na₂O and HRTEM image of resulting MoS₂ [53]. (d) Schematic illustration of the synthesis of MXene Ti₂CT_x by the LiF-HCl treatment of the MAX phase Ti₂AlC and TEM images for Ti₂AlC and Ti₂CT_x [59].

general formula of $M_{n+1}AX_n$, in which M represents an early transitional metal, and A represents one of the elements in Group 13 or 14, and X denotes C and/or N. The structure can be considered as stacked $M_{n+1}X_n$ layers connected by the A layers with metallic bondings. The selective etching of A layers from the MAX phase using concentrated HF or a mixture of an acid and a fluoride salt

has been proved to be effective ways for the bulk MAX phase exfoliation (Fig. 3d) [57–59]. Usually, the isolated MXene flakes own plenty of functional groups such as –OH, -F, making them negatively charged and well dispersed in water [58]. These functional groups not only facilitate the manufacturing of stable aqueous MXene solution but also enable the capability to adjust the

mechanical and electrochemical properties of MXene. A major challenge of MXene exfoliation is the utilization of HF or HF forming solution, which is not environment friendly. Developing non-HF and environmentally friendly etching methods is desirable and urgent.

2.3. Exchange strategies

For the transition metal oxides (TMOs) and double-layered hydroxides (LDHs) with strong ionic bonding between the host layers [60,61], the traditional mechanical cleavage, and chemical reaction assisted exfoliation strategies may not delaminate the layers without damaging the pristine structure or properties. For example, the oxidative agents or reductive alkali metals may not only break the interplane bonding but also damage the intraplane bonding. Alternatively, a two-step exchange-exfoliation strategy is used. The principle is expanding their interlayer gallery by the exchange of ions or molecules (Fig. 4a) and then exfoliate the expanded materials under a mild mechanical condition. For example, the interlayer alkaline cations can be exchanged by H⁺ cations, and hydrated protonic compounds will be formed when the TMOs are treated in an acidic solution. Then, the interlayer galleries will be further expanded by exchanging the hydrated protonic compounds with bulky organic ions, with the concomitant introduction of a large number of water molecules in this exchanging process. Such an exchange process and the generated water between the layers will significantly weaken the interlayer interaction, and the resultant product can be easily delaminated under mild stirring or ultrasonication conditions [62]. A similar process can also be applied to exfoliate LDHs, which represent a series of stacked octahedral hydroxide layers of divalent and trivalent metal ions as positively charged backbones and anions in the interlayer galleries. So far, many unilamellar TMOs and LDHs nanosheets have been successfully prepared by this method, such as manganese oxide (MnO_2) [63], tungsten oxide $(W_{11}O_{35})$ [64], ruthenium oxide (RuO₂) (Fig. 4b) [65]. Through the process, the 2D nanosheets can be delaminated into the one-unit cell with high yield because of the selectivity of chemical processes. Moreover, the pristine inplane crystal structure can be well-preserved due to the reaction process mainly happens in the galleries. Further improvement should be made to simplify the procedure and reduce the process-

In summary, all three categories of exfoliation methods will lead to large-scale 2D nanosheets that are in the form of a solution or can be dispersed in the solvent to form a solution. Each exfoliation method presents unique characteristics. The microcleavage is suitable for the exfoliation of 2D materials with weak interfacial interactions, such as graphene [36],TMDCs (e.g., MoS₂ [66], WS₂ [67], TaS_2 [68] etc.), some TMOs (e.g., α -MoO₃ [69,70], V_2O_5 [71,72]) and MOFs [73,74]. This mechanism is most cost-effective in producing 2D materials powders in high quantity. However, the random mechanical crushing leads to the broad size distribution of the nanosheet [75]. But with careful selection of solvent, the sonication method can help reduce the nanosheet thickness to monolayer [37]. The chemical reaction and exchange mechanisms can extend the exfoliating capability to the layered materials with stronger interlayer interactions. These strategies need special considerations according to the chemical composition of the pristine bulk materials. One remaining challenge for all exfoliation methods is the large lateral size distribution of the produced nanosheets because the crystals break along randomly distributed defects. To achieve high-performance devices, the nanomaterials in the solution usually need to be further sorted to similar sizes. Therefore, new technologies that can promote the size uniformity will be critical to promote solution quality and device repeatability. In addition, novel manufacturing technologies that can selectively utilize the nanosheet with different sizes will be an interesting direction to explore [76]. Furthermore, the chemical agents added to facilitate exfoliation or improve dispersion may influence the pristine properties of 2D nanosheets and present toxicity to environment and users. Therefore, developing economic and environment-friendly exfoliation strategies is still an urgent task

3. Solution-based assembly strategies

In this section, we will discuss the principles, characteristics, and challenges of solution-based assembly strategies in achieving 2DM-WESDs. The solution-based assembly strategies represent the assembly (or deposition) of 2D materials onto a target substrate from liquid solution or suspension. Note, the solutionbased mixing process for making composite will not be discussed here. The substrate can be in the formats of 1D fibers, 2D planar substrates (e.g., polymer film or metal foil), or 3D foams/scaffolds, as shown in Fig. 1. We can classify the assembly strategies into continuous strategies (Fig. 5) and discrete strategies (Fig. 6). Continuous strategies enable the continuous assembly process, which features high productivity but sometimes low accuracy (i.e., thickness control and lateral positioning in nanoscale resolution). Discrete strategies involve at least one isolated step in manufacturing processes, which usually have high assembly accuracy but relatively low productivity.

3.1. Continous assembly strategies

Representative continous assembly strategies are summerized in Fig. 5. The spray coating method is a widely used strategy to achieve coatings in both laboratories and industries. Its principle includes the atomization and spray of a nanomaterials solution towards the target substrate, where the nanomaterials film will be formed by the fast evaporation of the solvent, as depicted in Fig. 5a. Usually, the atomization process can be facilitated by high gas pressure and/or electrostatic process [77]. 2D materials spray coating can be applied to different substrates, such as carbon fiber veil [78], polydimethylsiloxane (PDMS) [79], polyethylene terephthalate (PET) [80], and polyimide (PI) [81]. The method requires a well-dispersed solution with controlled concentration and nanosheet size. In addition to the solution parameters, the processing conditions such as the nozzle type, gas pressure, distance, and angle between the nozzle and substrate can influence the atomization process and then the deposition quality [77]. Spray coating has several advantages. (1) The manufacturing process and equipment are cost-effective; (2) the process is easy to control; and (3) multilayer coating of different nanomaterials is possible. Spray coating faces the challenge of massive solvent evaporation and waste, which mainly increases the facility (should be processed in a well-ventilated facility) and supply cost. The evaporated solvent can hardly be recycled and will stress the environment. Developing non-toxic solutions and lean-solvent spray coating could be the future trend.

Inkjet printing utilizes the idea of printing, but the ink used is replaced by the 2D nanosheet solution, which is especially suitable for manufacturing patterned structures and devices. In this process, a 2D nanosheet solution is loaded into an ink reservoir, and the ink droplets will be extruded through a nozzle onto a target substrate (Fig. 5b). The unique features of inkjet printing include: (1) it generates patterned features directly without extra patterning steps, which can significantly reduce the manufacturing cost; and (2) this process can reach high-definition (~50 µm) assembly in the lateral dimension [82]. Ink printing has been applied to deposit 2D nanosheets such as graphene, MoS₂, and h-BN on PET

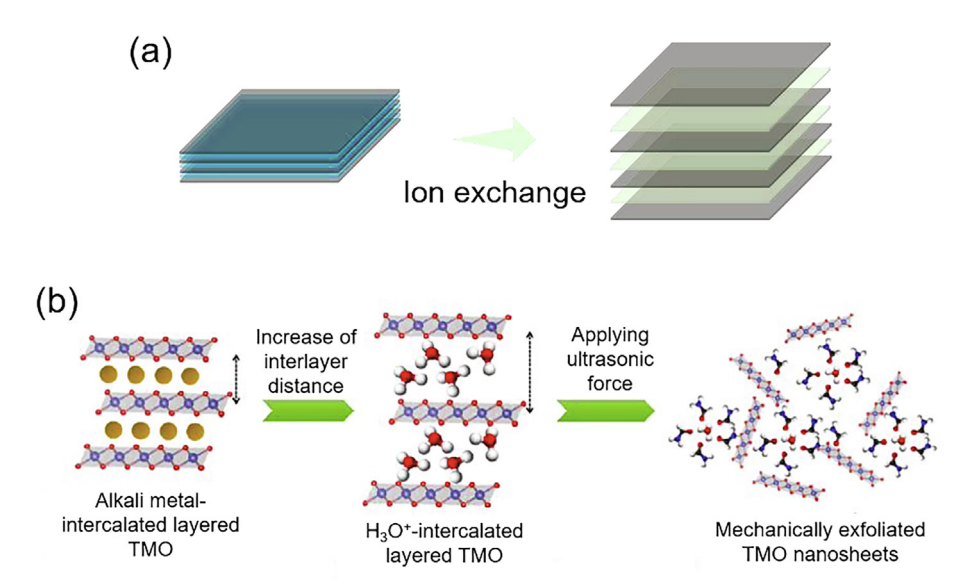


Fig. 4. Exchange exfoliation of 2D materials. (a) Schematic of ion exchange exfoliation. (b) Schematic diagram to the liquid exfoliation of ionic TMO material using hydronium-intercalated derivatives [65].

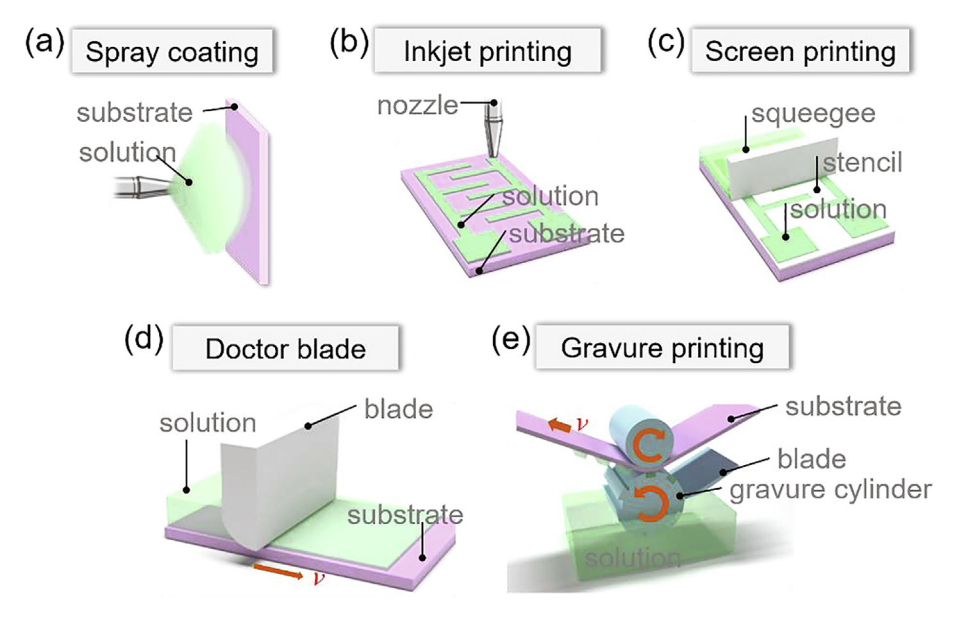


Fig. 5. The summary of the schematics of the solution-based assembly using continuous strategies.

substrate for applications such as transistors [83] and supercapacitors [84]. The non-contact printing process can also minimize the damage to the substrate caused by scratches. This feature is especially important when a flexible polymer substrate is used. To achieve stable and high-quality printing, the dispersion and rheology properties of the ink need to be considered carefully. The inks used for inkjet printing generally require a low viscosity (0.004–0. 03 Pa s) and a high surface tension (typically \sim 35 mN m⁻¹) [85], which can be varied for different printers. Moreover, there is a trade-off between resolution and productivity because a higher resolution usually needs delicate control of solution release. Employing multi nozzles printing is a future trend to achieve high throughput and maintain high resolution. Benefit from the high resolution and versatility, inkjet printing has been widely adopted to print flexible micro-supercapacitors [86,87] and has shown the promise to integrate with other solution-based assembly techniques. For example, by combining inkjet printing and spray coat-

ing, Kelly et al. fabricated a stacked all-solid graphene/ BN/graphene capacitor with areal capacitance ranges from 0.24 to $1.1~\rm nF~cm^{-2}$ on PET substrate [80].

Screen printing is a conventional printing technology originally used for printing circuit boards [88]. The typical process is illustrated in Fig. 5c. A stencil with etched motifs is placed above the target substrate, and the solution will be filled to one side of the stencil. The solution will fill the etched motifs by moving the squeegee against the stencil along the substrate, and the desired patterns can be formed. Compared to inkjet printing, the ink used in screen printing has a higher viscosity (0.05–5.0 Pa s) [89] and thus can be used to print thicker structures. Also, using a mask for the patterning allows a higher printing speed than the inkjet printing. This process can be fully adapted to roll-to-roll manufacturing by rotary screen printing [90]. Using this method, various patterned structures have been fabricated on planar flexible substrates using 2D nanosheets, such as graphene [91], graphene

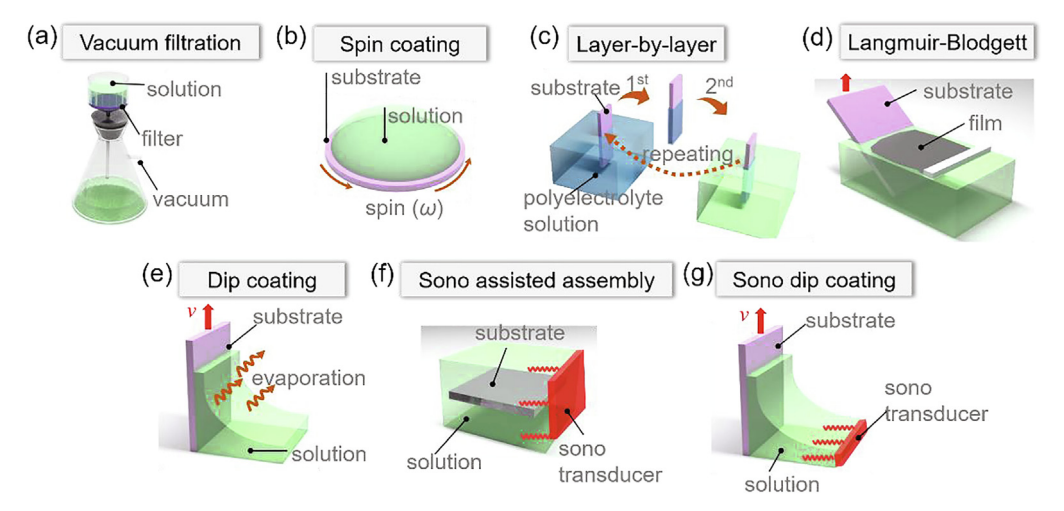


Fig. 6. The summary of the schematics of the solution-based assembly using discrete strategies.

oxide [92], MXene [93], etc. Utilizing a sacrificial layer as the printing substrate, Ng et al. transferred the printed patterns onto arbitrarily shaped 3D objects [94]. Usually, the conventional screen printing has a limited printing resolution of 40–150 μ m, and is restricted by the resolution of the stencil and the quality of the solution [95].

Doctor blade is also a traditional printing method that can be transformed to print 2D nanosheet solutions. A typical doctor blade system is composed of a movable stage, a substrate placed on the stage, and a doctor blade installed above the substrate (Fig. 5d). The gap between the doctor blade and the substrate will be used to control the deposition thickness. In the coating process. the 2D nanosheet solution will be poured onto the substrate surface. By moving the substrate, the doctor blade can remove the excess solution, and a thin and uniform layer of solution film will be formed on the substrate. This process is roll-to-roll compatible and has the promise to make the large-scale coating. This process can be performed at speed up to several meters per minute, and a wide range of wet film thickness from 20 to several hundreds of microns can be achieved by adjusting the gap between the doctor blade and the solution concentration [96]. In the doctor blade coating process, the immobilized blade may apply a unidirectional shear force to the solution that passes through the gap between the substrate and the blade and then leads to ordered alignment of nanomaterials (e.g., single-wall carbon nanotubes) [97]. Exploring and utilizing the 2D materials ordering using this technique might provide new opportunities for 2DM-WESDs.

Gravure printing is a highly efficient printing technology for patterned structure fabrication, which utilizes direct ink transfer through physical contact between the gravure cylinder and the substrates, as shown in Fig. 5e. The printing system consists of a gravure cylinder and a doctor blade. The gravure cylinder rotates in a bath of 2D nanosheet solution, filling the cells with the solution, and the excess fluid will be removed from the surface of the cylinder assisted by a doctor blade. Simultaneously, the flexible substrate slides between the two cylinders and allows for transferring of ink from the gravure cylinder onto the substrate resulting in printed features. Compared with other continuous processes such as inkjet printing and screen printing, gravure printing is a rollto-roll process that allows for higher printing speed up to 15 m s $^{-1}$ [90]. The gravure printing can provide high definition printing (as small as $\sim 2 \mu m$) [98]. Using this technique, Chang et al. demonstrated graphene printing on polyimide substrate for supercapacitors [99]. The supercapacitor cells can be controlled in various dimensions and depths at the same time. To make

high-definition printing, the solution rheology needs to be optimized and controlled. Usually, the solution with low shear viscosity in the range of 0.05–0.2 Pa s is used to prevent the possible solution to bleed out and allow higher line resolution [85]. The gravure printing may not be cost-effective for low-volume printing as the roller needs to be replaced when changing the pattern.

3.2. Discrete assembly strategies

A collection of discrete assembly strategies is summarized in Fig. 6. Vacuum filtration might be the simplest method for the fabrication of free-standing and flexible 2D nanosheets film. The 2D nanosheet solution passes through a filter membrane driven by the pressure difference created by a vacuum pump, and the 2D nanosheets will be retained over the membrane surface, as shown in Fig. 6a. Vacuum filtration is applicable for almost all the 2D nanosheet solutions and easy to manipulate. The thickness of the film can be varied between tens of nanometers to hundreds of microns and can be controlled by choosing membrane with different pore sizes and tailoring the concentration and volume of the solution [100]. Special attention should be paid when working with extremely thin or thick 2D nanosheet films. The ultrathin film creates challenges to release from the filter membrane. In contrast, the quality of the thick film might be affected by the fact that the stacked nanosheets can block the pores and reduce the filtration efficiency and film uniformity [101]. Also, filtration efficiency is affected by the high viscosity caused by high solution concentration. Thought this method is mainly used for manufacturing freestanding 2D nanosheet film, there are several interesting directions to explores. First, the method can be used to assemble 2D nanosheet (e.g., graphene) on the wall of holes in the filter membrane (e.g., cellulose paper) to construct a 3D flexible conductive film [102]. Second, direct device assembly might be achieved by patterning the filtration membrane as demonstrated in carbon nanotube devices fabrication [103]. Third, multilayer filtration that integrates the functionality of multiple 2D nanosheets is possible

Spin coating is a strategy to achieve film deposition by spreading the nanomaterial solution on a rotating substrate (Fig. 6b). It utilizes centrifugal force to distribute the deposited solution, and the film thickness can be controlled by adjusting the spinning speed, solution concentration, and spinning times [105]. In the semiconductor industry, it has been widely used for the coating of photoresist on silicon wafers. The spin coating is an accurately controlled process (i.e., acceleration and rotating speed) to achieve

uniform assembly with high reproducibility. For uniform spreading and deposition, the process requires good wetting among solvents, substrates, and 2D materials. For example, the hydrophilic treating of the wafer surface can effectively enhance the MXene-silicon adhesion and resulting in improved film integrity and uniformity [106]. When applied to 2DM-WESDs, the important considerations are matching 2D nanosheet solutions with suitable polymer substrate to enable good wetting. Furthermore, the thin polymer film substrate may not maintain the stable flat geometry under high-speed spinning because of the low rigidity. The viscosity of the solution should be adjusted to enable high fluidity over the substrate, and it is difficult to attain accurate control and high-quality film when the viscosity is too high or too low [107].

Layer-by-layer method is a subtle multilayer coating strategy that utilizes the electrostatic deposition. The operation is similar to the dip coating. Because the isolated 2D materials usually carry charges, by dipping a target substrate into a nanomaterial solution and then a polyelectrolyte solution with the opposite charges alternatively, the 2D material layer and polyelectrolyte layer can be formed layer by layer, as shown in Fig. 6c. The coating can be well-controlled in the thickness direction. Depending on the quality of 2D materials, assembly of one monolayer is possible. Furthermore, the assembly can be applied to non-planar substrates. This method is important for the manufacturing of thin-film electronics or optoelectronics with nanoscale resolution in the film thickness. However, the assembly process is time-consuming because of the low solution concentration and weak electrostatic interaction. New strategies to promote manufacturing efficiency will be desirable. To facilitate this process, Weng et al. developed a spin spray layer-by-layer (SSLbL) assembly strategy to assemble MXenecarbon nanotube composite film on the PET substrate rapidly. Different from the traditional layer-by-layer process, the nanomaterial solution was supplied by spray nanomaterials solution onto a rotated substrate [108].

In the Langmuir-Blodgett assembly, a monolayer and continuous 2D material film can be formed on the liquid-air or liquid-liquid interface by a compressing barrier. And then, a supporting substrate is used to scoop out the floating film for further applications (Fig. 6d). It is highly controllable for ultrathin film fabrication and has been applied to various 2D nanosheets, such as graphene, graphene oxide, MXene, and MoS₂ [109]. Using this method and cellulose film as a sacrifice substrate, Wang et al. fabricated a free-standing GO film (~22 nm) with melamine. This film synergizes the wrinkled GO nanosheets and strong noncovalent interaction between GO and melamine. The as-obtained film shows high optical transmittance (84.6% at 550 nm) and mechanical strength (45 MPa), and the reduced film shows promise in making highperformance ultrathin supercapacitors [110]. Petukhov and coworkers found that both the structures of the layers and assembly kinetics of MXene film at the liquid-air interface depend on the pH value of the solution. A ~ 1.5 nm monolayer MXene ($Ti_3C_2T_x$) film can be formed at pH > 4 [111]. This method does not rely on complicated facilities, but careful solution design and a stable manufacturing environment are desirable. A long-lasting challenge for the traditional Langmuir-Blodgett method is the poor scalability. To achieve large-scale manufacturing, some modified Langmuir-Blodgett strategies incorporating roll-to-roll coating equipment have also been demonstrated [112,113].

Dip coating has been widely used in coloring textile, coating food, glove fabrication, nanodevice fabrication in industrial applications, *e.g.*, medical, automotive, electrical, hand-tool, and consumer products [114]. Traditionally, dip coating assembly is a solvent evaporation-driven deposition process and achieved by dipping a substrate into the solution and withdrawing it at a constant rate. The particles will deposit at the solid–liquid-vapor contact line due to the oversaturation caused by solvent evaporation,

as shown in Fig. 6e. The film thickness can be controlled from a few nm to 1 μm using the same initial solution by adjusting the parameters (e.g., withdrawal speed) [115]. Dip coating has the advantages of simple equipment design, low solution waste, adaptability to different substrate sizes, and geometries (e.g., sheets, cylinders, and tubes) [116]. For complicated 3D patterned surfaces, changes in the flow of the coating solution during the withdrawal process may lead to inhomogeneous film thicknesses [117], which can be interesting strategies to control the hierarchical structures of the film [118]. The critical challenge to be solved for dip coating is increasing the dip-coating efficiency in terms of both assembly efficiency and withdrawal speed. For the graphene assembly on a poled PTFE surface, 15 times dip coating (10 s each) can only achieve 77% coverage [119]. Since the evaporation of solvents causes film formation, speeding up the evaporation process (e.g., using a volatile solvent, and/or heating up) can be a strategy to improve the assembly efficiency. Porous substrates such as cotton yarn [120], carbon cloth [121] have been widely adopted, because of their excellent flexibilities and adsorption capabilities. Understanding and carefully designing the interaction among 2D nanosheets, solvent, and substrate will be key to further increase productivity and controllability.

Sono assisted assembly (SAA) is a new method to achieve highrate and large-scale assembly of 2D nanosheets on polymer substrate [122]. Sono energy has been widely used to manipulate nanoparticles or bio cells in the solution [123]. Under the sonication, the dispersed nanoparticles can be focused and transferred by utilizing the acoustic force and streaming flow [124]. Perelshtein et al. have utilized the strong tip sonication to assemble various nanoparticles on the polymer substrate by sticking nanoparticles into the substrate, which will destroy the underline substrate [125]. Our group has developed a novel weak sonication-assisted assembly strategy for the assembly of 2D materials on flexible polymer substrate (Fig. 6f) [122]. By submerging the hydrophobic PDMS substrate into the graphene solution, conductive network can be formed in 10 seconds with the help of weak sono field (0.3 W/cm²). This strategy utilizes the design of surface energy, where the hydrophobic substrate and nanosheet form stable interface in a water environment. The weak sono field can significantly promote the assembly rate of 2D materials without damaging the substrates. A variety of 2D materials such as reduced graphene oxide, MoS₂, and h-BN have been successfully assembled. Furthermore, this strategy is also applicable for assembly on complex non-planar surfaces and 3D structures. It is important to note, SAA principle can be applied to transform existing technologies. As a proof of concept, we developed a sono dipcoating (SDC) method by integrating SAA with dip-coating process (Fig. 6g) [126]. The assembly happens under the water at the solidliquid interface. The dip-coating process provides shear stress that helps unify and speed up the assembly process. In contrast to evaporation driven dip coating, SDC eliminates the evaporation process as solution will not wet the substrate. Therefore, the withdrawal speed of substrate in SDC can reach 16 m/min, one to five orders of magnitude greater than that of existing nanomaterial dipcoating processes. It is also interesting to note that SAA is not only a new assembly principle, but also a self-healing method that can be used to reorganize and regenerate nanomaterial network and flexible electronis devices. Although discussed as discrete strategies here, dip coating, SAA, and SDC have the protential to be integrated with roll-to-roll process to realize continuous assembly.

In summary, significant efforts have been made to the highly-efficient, large-scale, and accurate assembly of reliable and high-performance 2DM-WESDs. To promote technology innovation, the researchers may consider the fundamental challenge for assembly 2D nanosheets on flexible substrates. First, there is a subtle balance among the three statuses of 2D nanosheets during the

assembly: staying in solution, assembling on the substrate, and aggregating in the solution. 2D nanosheet-solvent-substrate system presents complicated interactions among all three components leading to difficulty in designing the system. Second, the flexible substrate, especially polymer substrates, is not necessarily compatible with the solvent. For example, due to weak van der Waals forces among polymer chains, a good wetting solvent may dissolve and/or swell the polymer substrates. Besides, the solvents used for 2D nanosheet exfoliation and dispersion are usually toxic, presenting challenges for sustainable manufacturing. How to identify an efficient and sustainable 2D nanosheet-solvent-substrate system for assembly and drive the assembling of 2D nanosheets on the flexible substrates requires an in-depth understanding of the interaction among the three components. Note, solutionbased assembly is an interdisciplinary area requiring close collaborations among researchers from materials science and engineering, chemical engineering, chemistry, physics, and mechanics, This also represents the future opportunities for fundamental innovations in assembly technologies.

4. 2D materials for wearable supercapacitors

Supercapacitors are promising energy storage systems for fast power delivery or storage because of their exceptional power densities and cyclability. 2D materials have been widely accepted as emergent materials for wearable supercapacitor applications. One important strategy to achieve 2D materials-based wearable supercapacitors (2DM-WSs) is integrating 2D materials on flexible substrates, such as PET, PI, paper, carbon cloth, and PDMS. Typically, the 2D materials can be integrated with flexible substrates utilizing the solution-based assembly strategies directly or indirectly, and the resultant hybrid structures can be used as flexible electrodes for 2DM-WSs. For example, the exfoliated MXene nanosheets can be directly integrated with a flexible PET substrate through spray coating [127] and ink printing directly [87]. Alternatively, MXene film can be formed using vacuum filtration first and then transferred to the target substrate [128]. In this section, the state-ofthe-art achievements of 2DM-WSs, e.g., capacitance and cycling stability, will be discussed. Moreover, the flexibility (i.e., bendability and stretchability) of the wearable supercapacitor will be summarized and discussed.

4.1. The state-of-the-art energy storage performances of 2DM-WSs

Depending on the energy storage mechanism, the supercapacitors can be classified into two categories, i.e., electrochemical double-layer capacitors (EDLCs) and pseudocapacitors, as shown in Fig. 7a. In the charging process of EDLCs, one electrode is positively charged, and the other one is negatively charged. The anions in the electrolyte will be attracted to the positive electrode, and the cations will be attracted to the negative electrode. This process creates a "double-layer" at the interface between the electrode and electrolyte (Fig. 7a). For the pseudocapacitors, the energy is stored through fast surface redox reactions at the electrode-electrolyte interface. Due to the existence of chemical reactions, the pseudocapacitors show higher capacitance and energy density. But EDLC capacitors have higher charging rates and longer life cycles [129]. Despite the differences in the energy storage mechanism, the trend of supercapacitor research is to achieve higher capacitance, energy density, and longer cycling time with decreased cost. Tremendous efforts have been made to attain high-performance 2DM-WSs from new material development, surface design, electrode architecture design to manufacturing innovation [87,130-134]. For example, Wang et al. exfoliated a phthalocyanine-based 2D conjugated metal-organic frameworks (Ni₂[CuPc(NH)₈]) with an average lat-

eral size of \sim 160 nm (Fig. 7b) and mean thickness of \sim 7 nm (\sim 10 layers) through ball milling [135]. The fabricated device using Ni₂[-CuPc(NH)₈]/graphene electrode and PVA/LiCl gel electrolyte on polyimide substrate (Fig. 7b) shows outstanding cycling stability (91.4% of capacitance retention after 5,000 charging/discharge cycles) and high areal capacitance of 18.9 mF cm⁻² at the current density of 0.04 mA cm⁻². Xiao and co-workers developed a onestep interdigital mask-assisted fabrication of micro supercapacitor (Fig. 7c) [136]. With the assistance of a customized interdigital mask and vacuum filtration, the interdigital hybrid electrode based on layer-by-layer deposition of phosphorene and graphene can be directly manufactured and transferred to a flexible PET substrate as the flexible electrode. This simplified manufacturing strategy enables scalable fabrication of a serially interconnected supercapacitor pack (Fig. 7c), and the fabricated flexible shows excellent stability even under a folded state with an outstanding areal capacitance of 9.8 mF cm $^{-2}$ at 5 mV s $^{-1}$ (Fig. 7c).

To compare the overall performance of different 2DM-WSs, we have summarized the Ragon plot showing the energy density (the amount of energy that can be stored in a specific space) vs. power density (the speed of energy can be transformed in a specific space) in Fig. 7d and cycling stability, capacitance retention vs. cycling time, of various 2DM-WSs, in Fig. 7e. Ideally, both high energy density and power density are desirable by 2DM-WSs. In reality, there is a trade-off. Improving energy density is usually achieved by using pseudocapacitive materials. However, pseudocapacitive materials will introduce chemical reactions to the charging/discharging processes and lead to decreased charging/discharging rate and, consequently, lower power density. As shown in Fig. 7d, Orangi et al. demonstrated the highest energy density (51.7 μ W h c m⁻²) is achieved at a relatively low power density (5.7 mW cm⁻²) using the printed Ti₃C₂T_x on PET substrate [86]. Wang et al. showed that the highest power density (168 mW cm⁻²) is achieved in Ni₂[-CuPc(NH)₈]/graphene/PI system with a low energy density (1.1 μ W h cm⁻²) [135]. The synergy between the high energy density and power density requires sustained innovation in material discovery, structural design, and processing technology. Based on the energy storage mechanism, the potential direction can be developing materials and constructing structures with high electronic conductivity and increased open channels for fast transportation of ions and electrons [137].

The device cycling stability is another critical factor for the commercialization of 2D-WSs. In Fig. 7e, the capacitance retention vs. cycling time is summarized. We need to point out that this comparison can only provide a rough estimation since cycling stability is also strongly related to the charging/discharging rate. The more detailed information and comparison can be found in Table 1. Overall, the cycling stability is related to the material system (i.e., 2D materials, substrate, and electrolyte), the energy storage mechanism, and the device configuration. For the EDLC type electrode materials, there is no redox reaction and volume change, and therefore, they usually exhibit a longer cycling lifetime with lower energy density [129]. Furthermore, the combination of electrode materials can be tailored to achieve exceptional performance. Using Ti₃C₂T_x as the negative electrode and rGO as the positive electrode material, 97 % of the capacitance can be retained after 10,000 cycles at 0.2 mA cm⁻², while the all-MXene symmetric device faded down to 75 % after 10,000 cycles [127]. Exploring and improving the cycling stability under high rate charging/discharging will remain as a hot spot because of the needs of fast charging electronics and vehicles.

4.2. Flexible stability of 2DM-WSs

It is expected that 2DM-WSs will be conformly attached to human interface and can accommodate various deformations in

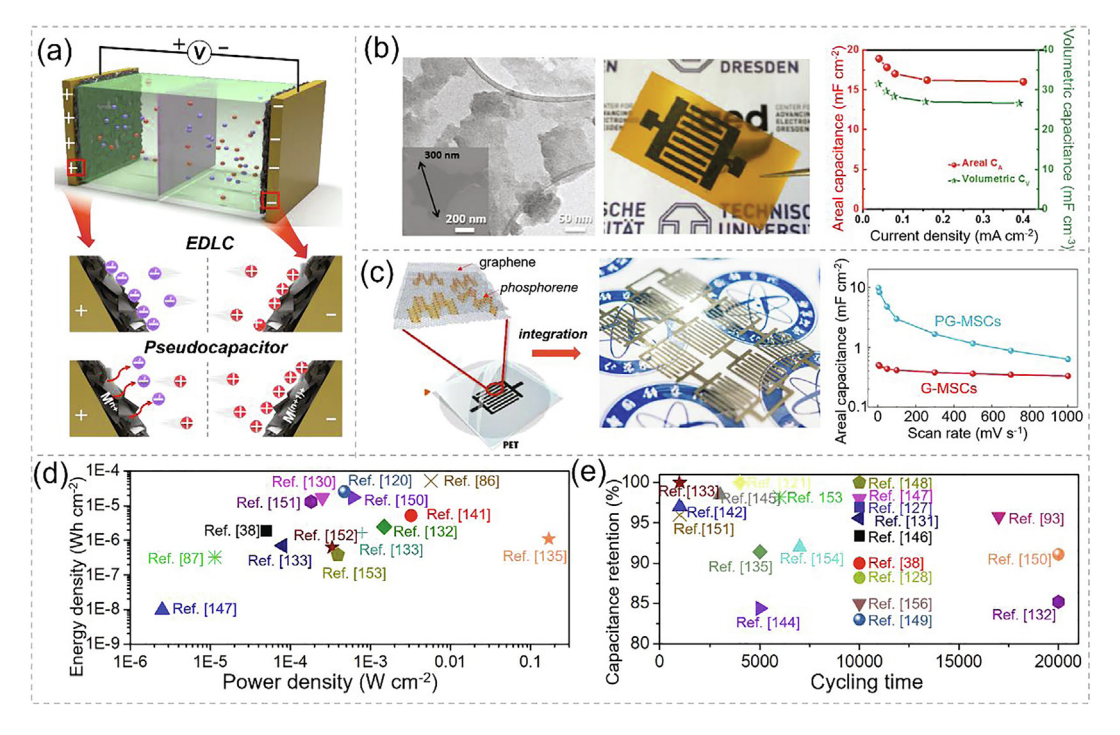


Fig. 7. The state-of-the-art achievements of 2DM-WSs. (a) Schematic illustration of the charging process in a basic EDLC supercapacitor and pseudocapacitor. (b) TEM image of exfoliated MOF through ball milling, the photo of the fabricated flexible electrode, and the device performance, respectively [135]. (c) Schematic of vacuum filtration assisted graphene/phosphorene electrode fabrication, the photo of a serially interconnected supercapacitor pack, and the device performance, respectively [136]. (d) Ragone chart showing energy density vs. power density for various 2DM-WSs. (e) Cycling stability for different 2DM-WSs.

daily activities. Therefore, to achieve reliable 2DM-WSs, it is desired to maintain the excellent electrochemical performance after cyclic deformations, such as repeated bending and stretching. Due to the high mechanical stiffness of 2D materials (e.g., \sim 1 TPa for graphene [138], \sim 3–75 GPa for dry MXene (TiC₂T_x) [139]), weak stiffness of polymer, low interfacial strength between 2D materials and polymer substrate, repeated mechanical deformations of 2DM-WSs may lead to conductive network damage and reconfiguration, and nanomaterial-substrate interfacial delamination.

Currently, bending, and stretching tests are widely used to evaluate the flexible stability of 2DM-WSs. The flexible stability is defined as the device performance retention (e.g., capacitance retention) after the bending or stretching cyclings. A typical bending cycling test is illustrated in Fig. 8a. The device performances will be monitored with respect to the different bending radius/or angles for different cycles. In Fig. 8b, we summarized the capacitance retention of various 2DM-WSs under the cyclic bending test with different test conditions, and detailed information can be found in Table.1. Dutta et al. studied the device performance under different bending angles from 0 to 180° using different TMOs (MoO₃, MoO₂, RuO₂)/SWCNT composite electrodes (Fig. 8c) [140]. They proved that the performance of the devices using the asprepared TMOs nanosheets/SWCNT composites are not only superior over previously reported TMOs based supercapacitors in terms of specific capacitance but also exhibit high stability under various bending angles from 0 to 180° (Fig. 8d). By incorporating PVA into the graphene ink, the adhesion between the printed pattern with the PI substrate can be increased and leads to 94.6 % capacitance retention after 10,000 bending cycles from 0 to 180° [141]. Hyun and co-workers performed the bending test with two different directions (Fig. 8e) for the printed graphene supercapacitor [142]. After 1000 bending cycles at a bending radius of 1 cm, the specific capacitance of the devices showed a negligible change, regardless of the bending direction (Fig. 8f). Unfortunately, there are no established standards to follow in such measurement where the sample thickness, bending radius, bending angle (e.g., $0^{\circ}-180^{\circ}$), and cycling number (e.g., 100-10,000) are all different. It is difficult to obtain a rigorous comparison. This also highlights an urgent need to establish a standard that can be acknowledged widely by this field.

Compared to the bending test with localized deformation, the stretching test will give global strain to 2DM-WSs, and the test is mainly focused on devices with polymer substrates. The stretchability is highly desirable to mimic the function of human skin and flesh. The device performance is usually evaluated through a cyclic stretching/releasing test (Fig. 8a), and the performance will be monitored under different strains or different cycling times with a certain strain. In Fig. 8g, we summarized the flexible stability under long-time stretching cycles with different strains, and the detailed information can be found in Table.1. Significant progress has been made towards developing novel structures and materials for improving stretchability while maintaining high specific capacitance. To date, the deposition of 2D materials on pre-stretched substrates to form a buckled or wavy structure represents a promise and successful strategy to attain high stretchability [143]. Recently, Moon et al. coated GO on a pre-stretched Ecoflex sponge substrate, and whereafter the GO was reduced using hydriodic acid vapor [144]. After coating PEDOT: PSS and PVA/H₂SO₄ gel and releasing the pre-stretch, a short periodic wavy structure was formed (Fig. 8h). The fabricated devices show excellent stretching stability with 85.1% capacitance retention at 300% strain. Even after 500 cycles stretching at 300%, 75.5% of the capacitance can be retained (Fig. 8i). Chang and collaborators fabricated crumbed MXene nanocoatings using pre-stretched VHB acrylic tapes (Fig. 8j) [145]. The accordion-like structure can be reversibly folded/unfolded by in-plane deformations and thus can sustain large strain. The fabricated device shows excellent electrochemical stability. 93% of the specific capacitance can be preserved under 100% strains after 3000 charge-discharge cycles, which is comparable to the unstrained sample of 98% retention (Fig. 8k). Similarly,

Table 1Summary of recently reported wearable supercapacitors using exfoliated 2D materials as electrode materials.

System	Substrate	Methods	Energy storage performance				Flexible Stability		Ref.
			Capacitance	Energy density	Power density	Cycling CR/#/condition	Bending CR/#/condition	Stretching CR/ #/condition	_
Graphene/ phosphorene	PET	Filtration	~9.8 mF cm ⁻² /5 mV s ⁻¹	11.6 mWh cm ⁻³	1.5 W cm ⁻³	-	89.5 %/2,000/c180°	-	[136]
Graphene	PET	Spray	$6.6 \text{ mF cm}^{-2}/1 \text{ mV s}^{-1}$	0.98 mWh cm ⁻³	2.1 W cm ⁻³	93.4 %/10,000/200 μA cm ⁻²	93 %/1,000/0-180°	_	[146]
Gzraphene	Paper	Screen	68.2 mF cm ⁻² / 0.5 mA cm ⁻²	0.0019 mWh cm ⁻²	$0.05~\rm mW~cm^{-2}$	90 %/10, 000/0.5 mA cm ⁻²	-	-	[38]
Graphene	PI	Gravure	37.5 mF cm ⁻² /5 mV s ⁻¹	5.2 μ Wh cm ⁻²	3.2 mW cm ⁻² ,	_	94.6 %/10,000/0-180°	_	[141]
Graphene	PET	Ink printing with flow	$268 \mu F \text{ cm}^{-2}/10 \text{ mV s}^{-1}$	-	-	97 %/1,000/1 V s ⁻¹	100 % / 1,000/r = 1 cm	-	[142]
Graphene	PET/Ag	Electrodeposition	$0.3~{ m mF~cm^{-2}}/0.1~{ m V~s^{-1}}$	9.7 nWh cm ⁻²	$2.5~\mu W~cm^{-2}$	98 %/10,000/ 0.024 mA cm ⁻²	-	-	[147]
Graphene/Fe ₃ O ₄	CC	Dip coating	~53F g ⁻¹ /1A g ⁻¹	19.2 Wh kg ⁻¹	$800.2~{ m W~kg^{-1}}$	100 %*/4,000/1 A g ⁻¹	100 %*/1/0-180°	_	[121]
Graphene/PANI	Paper	Spreader	123 mF cm ⁻² /20 mV s ⁻¹	17.1 μWh cm ⁻²	0.25 mW cm ⁻²	-	74.8 %/500/0–120°	_	[130]
Graphene/PANI	PDMS	Transfer	429 mF cm ⁻² /1 A g ⁻¹	77.8 Wh kg ⁻¹	995 W kg ⁻¹	95.6 %/10,000/5A g ⁻¹	100 %*/1/0-90° (finger bent)	91.2%/100/0-100%	[131]
rGO/PEDOT: PSS	Ecoflex	Absorbing	38.7 mF cm ⁻² /0.1 A g ⁻¹	11.44 Wh kg ⁻¹	131.58 W kg ⁻¹	84.4 %/5,000/0.25 A g ⁻¹	=	75.5%/500/0-300%	[144]
AgNWs-MoS ₂	PET	Spray	27.6 mF cm ⁻² /0.2 V s ⁻¹	2.453 μWh cm ⁻²	1.472 mW cm ⁻²	85.2 %/20,000/0.5 V s ⁻¹	98.6 %/100/0-180°	_	[132]
$MoO_2/Ti_3C_2T_x$	PET/Au	-	14.6 mF cm ⁻² / 0.05 mA cm ⁻²	$0.7~\mu Wh~cm^{-2}$	80 μW cm ⁻²	100 %/1,000/ 0.2 mA cm ⁻²	100 %*/1/0-150°	-	[133]
$Ti_3C_2T_x$	Textile	_	759 mF cm ⁻¹ /2 mV s ⁻¹	_	_	100 %/10,000/30 mA cm ⁻¹	_	100%*/2000/-14.1%	[148]
$Ti_3C_2T_x/MoO_2$	CC	_	511.2F g ⁻¹ /1A g ⁻¹	29.58 Wh kg ⁻¹	$749.92~{\rm W~kg^{-1}}$	83 %/10,000/5A g ⁻¹	_	-	[149]
MoS ₂ /Ti ₃ C ₂	CC	-	347 mF cm ⁻² /2 mA cm ⁻²	17.4 μWh cm ⁻²	600 μW cm ⁻²	91.1 %/20,000/ 30 mA cm ⁻²	100 %*/1/0-0-180°	-	[150]
$Ti_3C_2T_x$	CC	Direct drop	362 mF cm ⁻² /2 mV s ⁻¹	$13 \mu Wh cm^{-2}$	$181 \mu W cm^{-2}$	96 % / 1,000 /10 mV s ⁻¹	100 %*/1/0-120°	_	[151]
$Ti_3C_2T_x$	PET	Brushing/stamping	61 mF cm $^{-2}/25 \mu A \text{ cm}^{-2}$	$0.63~\mu Wh~cm^{-2}$	0.33 mW cm ⁻²	93.7 %/10,000/200 μA cm ⁻²	85 %/1,600/0-180°	-	[152]
$Ti_3C_2T_x$	PET fiber	Electrospinning	18.39 mF cm ⁻² /50 mV s ⁻¹	$0.38 \mu Wh cm^{-2}$	0.39 mW cm^{-2}	98.2 %/6,000/50 mV ⁻¹	100 %*/1/0-180°	_	[134]
$Ti_3C_2T_x$	Cotton yarn	Dip coating	519 mF cm ⁻² /2 mV s ⁻¹	$25.4~\mu Wh~cm^{-2}$	0.47 mW cm ⁻²	100 %/10,000/20 mV s ⁻¹	-	-	[120]
$Ti_3C_2T_x$	Paper	Screen printing	158 mF cm ⁻² / 0.08 mA cm ⁻²	$1.64~\mu Wh~cm^{-2}$	778.3 μW cm ⁻²	95.8 %/17,000/-	-	-	[93]
$Ti_3C_2T_x$	PI	Screen printing	70.1 mF cm ⁻² /10 mV s ⁻¹	0.42 mWh cm^{-2}	_	92 %/7, 000/5 mA cm ⁻²	100 %*/1/0-90°	_	[153]
$Ti_3C_2T_x$	PET	Spray	$2.4 \text{ mF cm}^{-2}/2 \text{ mV s}^{-1}$	8.6 mWh cm^{-3}	$0.2 \ {\rm W} \ {\rm cm}^{-3}$	97 %/10,000/0.2 mA cm ⁻²	100 %*/1/0-180°	-	[127]
Ti ₃ C ₂ T _x /MWCNT	PCL	Spray-layer-by- layer	80 mF cm ⁻² /10 mV s ⁻¹	-	-	-	-	-	[154]
$Ti_3C_2T_x$	PET/paper	Printing	$1.03 \text{ mF cm}^{-2}/2 \text{ mV s}^{-1}$	$51.7 \mu Wh cm^{-2}$	5.7 mW cm^{-2}	_	100 %*/1/0-180°	_	[86]
$Ti_3C_2T_x$	PET/PI	Printing	43 mF cm $^{-2}/20$ mV s $^{-1}$	$0.32~\mu Wh~cm^{-2}$	$11.4~\mu W~cm^{-2}$	97 %/10,000/14 μA cm ⁻²	-	-	[87]
$Ti_3C_2T_x$	PET	Vacuum filtration	356.4 mF cm ⁻² / 0.2 mA cm ⁻²	79.2 mWh cm ⁻³	0.4 W cm ⁻³	88.2 %/10,000/ 1.5 mA cm ⁻²	92.2 %/100/0-120°	-	[128]
$Ti_3C_2T_x$	VHB tape	Vacuum filtration	95F cm ⁻³ /25 mV s ⁻¹	5.5 Wh g^{-1}	0.5 kW kg^{-1}	98.5 %/3,000/10 A g ⁻¹	100 %*/1/0-180°	76 %/1000/80 %	[145]
$Ti_3C_2T_x/rGO$	VHB tape	Vacuum filtration	18.6 mF cm ⁻² /0.1A g ⁻¹	-	=	85 %/10,000/1 A g ⁻¹	=	92 %/1/300%	[155]
Ti ₃ C ₂ T ₂ /graphene	CC	Spray	54 mF cm ⁻² /0.1 mA cm ⁻²	_	_	100 %/1,000/0.1 mA cm ⁻²	_	_	[156]
MoO ₃ /SWCNT	PET/Au	Filtration	1205.08F g ⁻¹ /5 mV s ⁻¹	24.89 Wh kg ⁻¹	1.61 kW kg ⁻¹	91.99 %/1,000/100 mV s ⁻¹	100 %*/1/0-180°	_	[140]
MoO ₂ /SWCNT	PET/Au	Filtration	1168.69F g ⁻¹ /5 mV s ⁻¹	18.73 Wh kg ⁻¹	1.21 kW kg ⁻¹	95.88 %/1,000/100 mV s ⁻¹	100 %*/1/0-180°	-	[140]
RuO ₂ /SWCNT	PET/Au	Filtration	1308.45F g ⁻¹ /5 mV s ⁻¹	23.84 Wh kg ⁻¹	1.52 kW kg ⁻¹	92.25 %/1,000/100 mV s ⁻¹	100 %*/1/0-180°	=	[140]
Ni ₂ [CuPc (NH) ₈]/graphene	PI	Filtration	18.9 mF cm ⁻² / 0.04 mA cm ⁻²	1.1 μWh cm ⁻²	168 mW cm ⁻²	91.4 %/5,000/0.4 mA cm ⁻²	86.2 %/3,000/0-90°		[135]

Notes: CR represents the capacitance retention. #, the cycling time. CC: carbon cloth. r: bending radius. -, not available. CR = 100% * is used when the authors claimed negligible change, no change, or stable performance during or after the flexible test. Therefore, it cannot be used for quantitative comparison.

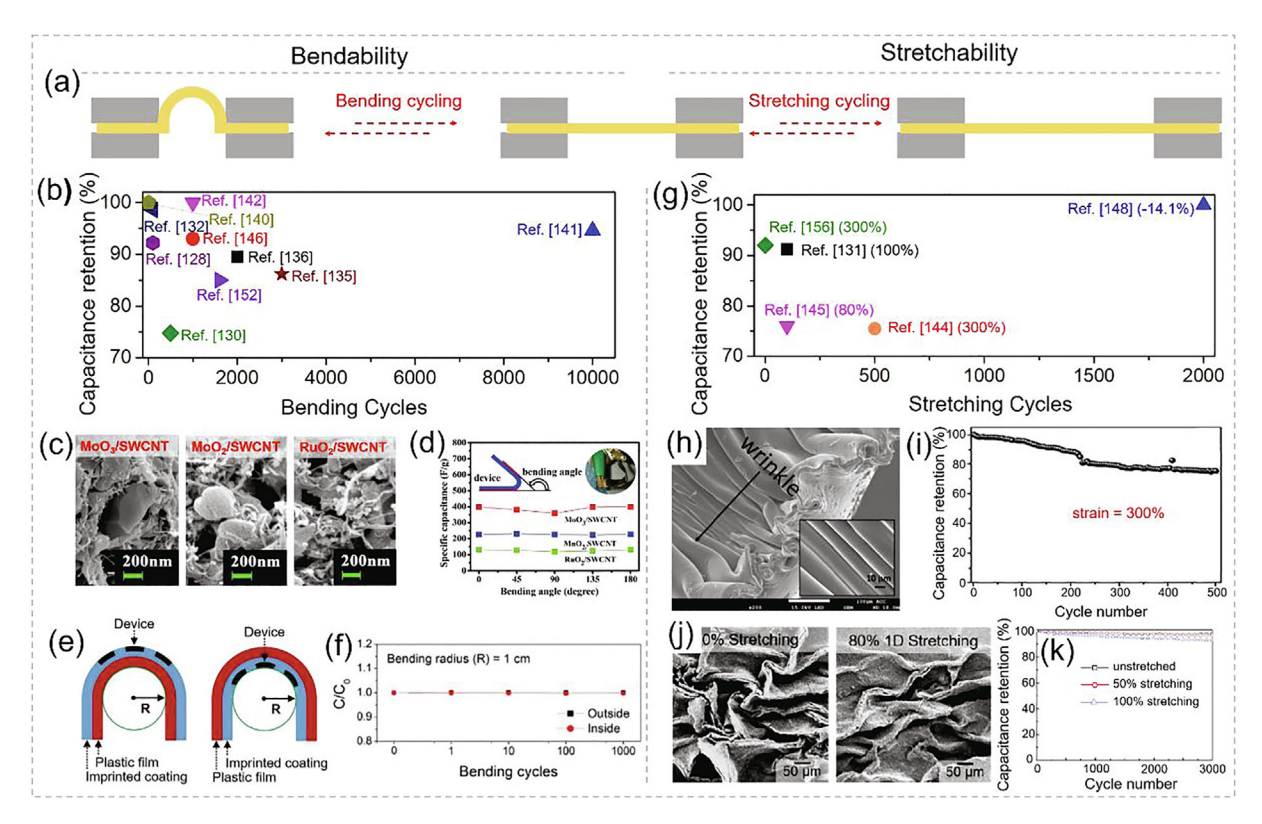


Fig. 8. The flexible stability measurement of 2DM-WSs. (a) Schematic showing the cycling bending and stretching. (b) Summarized capacitance retention after different bending cycles. (c) The SEM images of different TMOs/SWCNT composites and the corresponding flexible supercapacitor devices performance under different bending angles (d) [140]. (e) Schematic illustrations for outside and inside bendings. (f) The relative specific capacitance over 1,000 cycles of bending the devices outside and inside the substrate at a bending radius (r) of 1 cm [142]. (g) Summarized capacitance retention after different stretching cycles. (h) SEM images of the PEDOT: PSS/rGO/Eco wavy structure, and (i) the flexible stability under repeated stretching and releasing for 500 cycles [144]. (j) Top-down SEM images of crumpled MXene nanocoatings at 0% and 80% 1D stretching states. (k) Flexible stability of stretchable MXene electrodes after multiple stretching/relaxation cycles (1000 cycles of 50% and 80% 1D stretching) [145].

the stretching test suffers from the lack of a unified test standard where the specific geometry, strain, and cycling number should be fixed.

5. 2D materials for wearable batteries

Different from supercapacitors, the batteries store energy via different Faradaic reactions on the electrodes, which are usually accompanied by a phase transformation in the electrode materials. For example, in the Li⁺ or Na⁺ batteries, the energy is stored by the insertion of Li⁺ or Na⁺ ions from the cathode to the anode when charging, as shown in Fig. 9a. To achieve high energy storage performance, the materials used in the electrodes require excellent reversible energy storage capacity, high electronic and ionic diffusivity, and excellent structural stability upon phase transformations during the charging/discharging cycles (Fig. 9h) [157-160]. 2D nanosheets such as graphene, MoS₂, MXene, and MOF, have shown ultrahigh conductivity, large specific surface areas, and low surface diffusion barriers that make them the superior candidates for the next generation of wearable batteries [161–165]. Also, the hybrid structures containing 2D nanosheets have been explored as electrode materials with exceptional properties [166]. In this section, the state-of-the-art energy storage achievements will be discussed first. Following this, the flexibility of 2D materials-based wearable batteries (2DM-WBs) will be evaluated.

5.1. The state-of-the-art energy storage performances of 2DM-WBs

Via solution-based methods, 2D materials can be assembled on different flexible substrates, such as carbon cloth, nylon mem-

brane, metal foil, and melamine foam, to form the wearable electrodes of batteries [167–170] (Table 2). To overcome the shortcomings of weak bonding force, volume effect and uncontrollable dendritic growth, hybrid nanomaterials with hierarchical nanostructures are also designed.

Among different combinations, the MXene-metal foil system presents the highest capacitance and charge-discharge cycling stability. Due to the good electric contact, short diffusion distances. and reasonable accommodations for volume changes, the metal foil substrates are widely used in 2DM-WBs. For example, Zhang et al. demonstrated assembling nSi/Ti₃C₂T_x on Cu foil via slurryand the highest initial reversible capacitance (\sim 3200 mAh g⁻¹ at 0.15 A g⁻¹) was achieved (Fig. 9b) [171]. Also, its capacitance remains stable after 8 cycles (Fig. 9c). As an effective binder, the introduction of MXene forms a continuous metallic network, enables fast charge transport, and provides good mechanical reinforcement. Similarly, the cycling performance is obtained by assembling $Ti_3C_2T_x$ on a stainless steel substrate. For example, Shen et al. demonstrated the Ti₃C₂T_x with Li plating can be assembled on stainless steel through 3D printing (Fig. 9d) [172]. The MXene-Li/LFP battery remains 99.4 % of capacitance after 300 cycles at 1C (Fig. 9e). MXene arrays with largely available interspaces not only facilitate the nucleation of lithium and homogenize both lithium ion flux and electric field, efficiently inhibiting the growth of lithium dendrites, but also provide enough space to accommodate the growth of massive cobblestone-like lithium. Besides, other 2DM such as graphene with high conductivity can be used. Bai et al. developed a Li-metal battery through directly assembling graphene on lithium foil using spray coating [169]. The energy storage performance reveals that an initial reversible

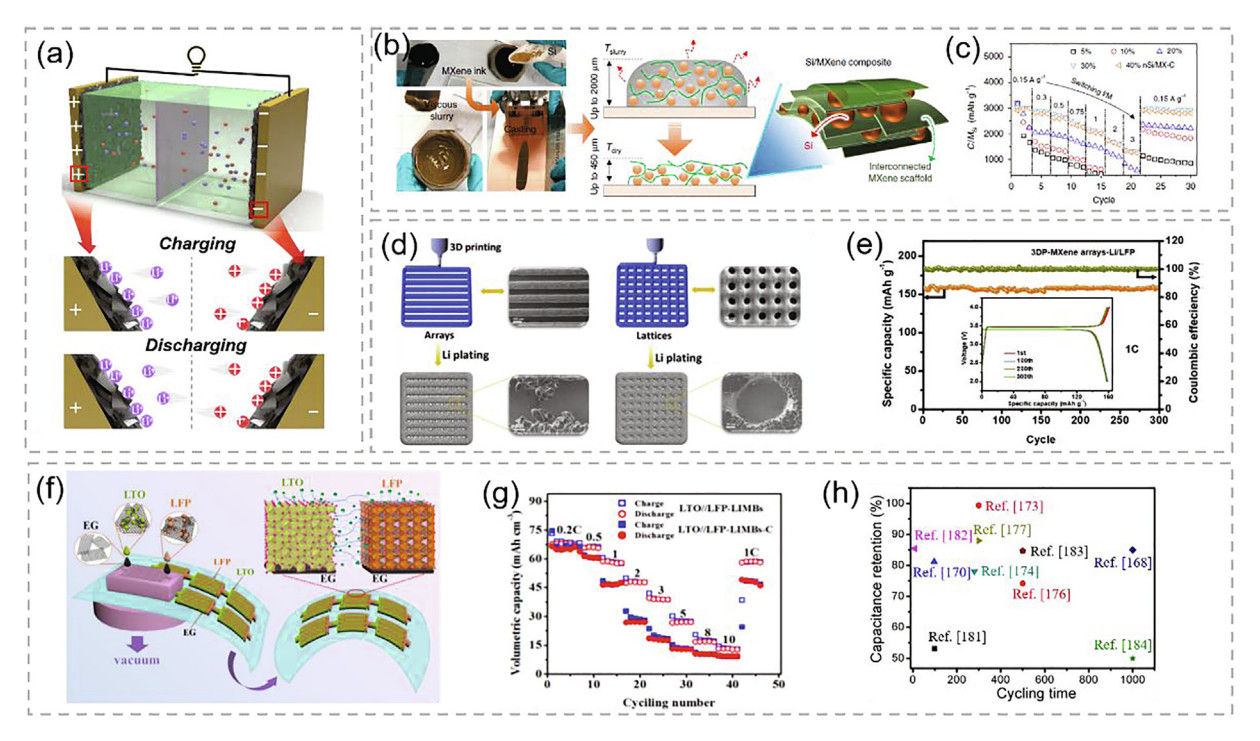


Fig. 9. The state-of-the-art energy storage performances of 2DM-WBs. (a) Schematic of the energy storage mechanism of batteries. (b) Si/MXene composite electrode prepared by the slurry-casting method. (c) Rate performance of nSi/MX-C electrodes [171]. (d) Schematic of 3D printing MXene arrays and lattices. (e) Cycling stability of MXene arrays-Li/LFP [172]. (f) Schematic illustrating the mask-assisted fabrication of integrated LTO//LFP-LIMBs. (g) Rate capability of LTO//LFP-LIMBs [168]. (h) Summary of cycling performance of 2DM-WBs.

capacitance of 130.1 mAh g $^{-1}$ at 1C is achieved, and reduces to 5 mA cm $^{-2}$ after 1000 cycles. Such a battery can also be manufactured by combining a roll-to-roll method to realize a large-scale and continuous electrode. These solution-based strategies endow the batteries with high reversible capacitance and stable cycling performance due to the robust 2D architecture and less dendritic growth.

The challenges for using metal foil include limited flexibility (the foil may crack under repeated bending cycle and can be hardly stretched) and weak 2DM-substrating bonding [173]. For example, Fu et al. designed a graphene-based ink, which can be assembled on Al foil via 3D-printing. For the integrated battery, only 78 % of capacitance retention was obtained after 280 cycles, which is ascribed to the relatively weak interfacial bonding [173]. To improve battery flexibility, the development of 2DMs-on-polymer 2DM-WBs is quickly catching up.

All-solid-state planar lithium-ion micro-batteries (LIMB) represent a new trend due to the requirement of less liquid electrolyte leakage, safety, and flexibility [174]. Zheng et al. fabricated a LIMB by assembling graphene on a nylon membrane using mask-assisted vacuum filtration (Fig. 9f) [168]. The resulting LIMB delivers an ultrahigh volumetric energy density of 146.3 mWh cm⁻³ with a power density of 8.8 W cm⁻³. Also, it presents a reversible capacitance of 67.7 mAh cm⁻³ at 0.2C, and there is no capacitance loss after 3300 cycles at 5C. The outstanding rate capability can be attributed to the multi-directional Li-ion diffusion mechanism (Fig. 9g).

5.2. Flexible stability of 2DM-WBs

Providing a stable power supply during deformation is a critical challenge for 2DM-WBs, and it is surprising to notice that there were only limited attempts. Though there is no unified standard to follow, the researchers are exploring different ways to demonstrate the flexible stability of the devices. Most of the tests are focusing on bending. Some researchers tried to monitor the light

intensity of the LEDs powered by the 2DM-WBs at different bending angles and after several bending cycles [175,176]. For example, Sang et al. constructed a 3D graphene nanosheet/SiOC_f//LiFePO₄ battery that sustains stable lighting of the connected LEDs under different bending angles (e.g., 45°, 90°, 180°) (Fig. 10a and b) [175]. Tang et al. assembled $Ti_3C_2T_x$ on iodine modified carbon cloth (CC-I) by the drop-filtration method to develop a quasisolid-state battery [167]. Even under a repeated flat-bending-flat state, a red LED lamp can be steadily powered, which may be attributed to the strong adhesion between MXene and CC-I. Deng et al. demonstrate a flexible LIB full cell (MoS2@C/ carbon cloth // LiCoO₂/Al) that can still power the LED after 300 bending cycles (Fig. 10c-e)[177]. Some researchers tried to monitor capacitance retention. For example, bending-durable batteries are achieved by electroplating Ti₃C₂T_x MXene on carbon cloth (CC) (Fig. 10f) [176]. The full battery assembled by Na-Ti₃C₂T_x-CC electrode (Fig. 10g) and NVP performs high capacitance retention of 88% (at the current density of 500 mA/g) after 300 cycles under 90° bending state, which is the same as the one at steady state (Fig. 10h). It implies that Na-Ti₃C₂T_x-CC possesses high bending durability. Even at the 270° bending state, there is still a high capacitance retention of 89% (Fig. 10h). The electroplating process enhances the binding force between Ti₃C₂T_x and CC, which prompt Ti₃C₂T_x efficiently to induce Na's initial nucleation and laterally oriented deposition and avoid generating mossy/dendritic Na [178]. The most exciting result is presented by Zheng et al., using the vacuum filtration method to build a planar graphene-based battery [168]. After 10,000 bending cycles at 180°, the capacitance remains ultra-stable that only slight capacitance fluctuation appears. The integrated structure features no structural degradation or interfacial delamination between microelectrodes and substrate.

Compared to wearable supercapacitors, the flexible stability of 2DM-WBs is facing a new challenge of phase changes caused by the dynamic charging and discharging reactions, in addition to the relatively weak heterogeneous interface between 2D nanomaterials and flexible substrate. For example, using $Ti_3C_2T_x$ as an elec-

Table 2Summary of recently reported 2DM-WBs.

System	Substrate	Methods	Energy storage performance	Flexible stability	Ref.			
			Initial reversible capacitance	Energy density	Power density	CR/#/condition	Bending CR/ #/condition	
LTO/graphene	Nylon membrane	Vacuum Filtration	67.7 mAh cm ⁻³ /0.2C	146.3 mWh cm ⁻³	8.8 W cm ⁻³	~100 %/3300/5C	100 %*/10000/ 0-180°	[168]
Si@RGO	Carbon fiber paper	Soaking	$2055 \text{ mAh g}^{-1}/100 \text{ mA g}^{-1}$	-	-	53.1 %/100/ 100 mA g ⁻¹	-	[180]
Graphene	SiOC _f cloth	Vacuum filtration	924 mAh $g^{-1}/0.1~A~g^{-1}$	-	-	74.2 %/500/ 0.5 A g ⁻¹	100 %*/1/45°, 90°, 180°	[175]
V ₂ O ₅ / Graphene	CNT paper	Spray coating	396 mAh g ⁻¹ /0.1C	-	-	81.2 %/~97/1C	96.7 %/3/0-180°	[179]
GO	Li film	Spray coating	130.1 mAh g ⁻¹ /1C	-	-	100 %*/1000/5 mA cm ⁻²	-	[169]
S-graphene/g- C ₃ N ₄	Al foil	Spray coating	927 mAh g ⁻¹ /0.2C	-	-	78 %/280/0.2C	-	[173]
LTO/GO and LFP/rGO	Glass	Ink printing	117 mAh $g^{-1}/50$ mA g^{-1}	-	-	~85.5 %/10/ 50 mA g ⁻¹	-	[181]
MoS ₂ @C	CC	Electrostatic attraction	1130 mAh g^{-1} and 3.428 mAh cm $^{-2}$ /0.1 mA cm $^{-2}$	-	-	-	100 %*/300/ bending	[177]
$Ti_3C_2T_x$	Na-CC	Electroplating	115 mA h $g^{-1}/100$ mA g^{-1}	-	-	88 %/300/ 500 mA g ⁻¹	88 %/300/90° 89 %/300/270°	[176]
$Ti_3C_2T_x$	Carbon cloth/I 125 W kg ⁻¹	Drop-filtration	330 mA h g ⁻¹ /0.5C	1050 Wh kg ⁻¹		C	, ,	
	85 %/1000/ 0.5C		100 %*/repeated flat-bent-flat test	[167]				
$Zn-Ti_3C_2T_x$	Cu foil	Roll-to-roll and spray coating	158 mA h g ⁻¹ /0.2C 150 mA h g ⁻¹ /0.5C	-	-	~84.7 %/500/10C	-	[182]
nSi/ Ti ₃ C ₂ T _x	Cu foil	Slurry-casting	~3200 mAh g ⁻¹ /0.15 A g ⁻¹	-	-	100 %*/8/ 0.15 A g ⁻¹	-	[171]
$Ti_3C_2T_x$	Melamine foam	Soaking	50 mAh cms ⁻² /50 mA cm ⁻²	-	-	100 %*/1900/ 50 mA cm ⁻²	-	[170]
$Ti_3C_2T_x$	Stainless steel/Li	3D printing	149.4 mA h g ⁻¹ /1C	-	-	99.4 %/300/1C	-	[172]
MIL-88A@S/ CB/PVDF	cc	Doctor blade	400 mA h g ⁻¹ /0.5C	-	-	50 %/1000/0.5C	-	[183]

Notes: CR: capacitance retention. #, the cycling time. -, not available. LTO, lithium titanate. LFP, lithium iron phosphate. SiOC₆, silicon oxycarbide ceramic fiber. CC, carbon cloth. CB, carbon black. nSi, nanoscale Si. CR = 100% * is used when the authors claimed negligible change, no change, or stable performance during or after the flexible test. Therefore, it cannot be used for quantitative comparison.

trode to suppress the generation of mossy/dendritic Na leads to capacitance retention of 89 % after 300 bending cycles [178]. A 96.7 % of capacitance retention can also be achieved after 3 bending cycles at 180° for graphene assembled on CNT paper as electrode [179]. Clearly, the study on the flexible stability of 2DM-WBs is at a very early stage and presents significant opportunities. The interdisciplinary collaboration, as well as the community-wide conversation to establish the testing standard, will be desirable to boost its development.

6. Conclusions and perspectives

In summary, the field of 2DM-WESDs is developing rapidly. In this review, we have summarized the recent progress of 2DM-WESDs from 2D nanosheet solution preparation, solution-based assembly technologies to the resultant wearable supercapacitors and batteries. The solution-based assembly is a promising route to achieve large-scale and affordable manufacturing of 2DM-WESDs. The explorations of 2DM-WESDs have demonstrated their potential to achieve flexible supercapacitors and batteries with superior energy storage capability and flexibility. These studies also help us define the challenges and opportunities for future development.

From a manufacturing perspective (Fig. 11), each assembly method has its unique advantages and limitations. In general, the synergy between assembly rate and accuracy is a long-lasting challenge that should be resolved. Moreover, it is challenging to identify the efficient and sustainable 2D nanosheet-solvent-substrate

system for different assembly methods. Further, the trend of sustainable and eco-friendly manufacturing desires new manufacturing technologies to reduced organic solvent usage/waste, minimized nanomaterial usage/waste, and recycle, regenerate, and reuse the devices. To fundamentally resolve these challenges, a comprehensive and interdisciplinary effort is desirable to understand, design, and predict the interaction among nanomaterials, solvent, and flexible substrates in complex material systems and assembly environments.

From the device performance perspective (Fig. 11), the resultant hierarchical structures of 2D nanosheet and the interface between the 2D nanosheet and substrate dictate the energy storage performance as well as the flexible stability of 2DM-WESDs. One critical challenge is that the ideal structure of 2D nanosheet for a highperformance device might not be readily achievable. For example, preferential alignment of 2D nanosheets is desirable but difficult to control in the energy storage process. A synergy among material synthesis, structural design, and manufacturing is desirable. The intrinsic property mismatch at the interface between 2D nanosheets and flexible substrates represents another key challenge to promote stability of the devices in both energy storage and flexibility. Engineering the interface should be leveraged with consideration from manufacturing viability. It is also important to note that flexible stability measurement has not reached a universal standard that required a systematic effort from multiinterdisciplinary communities.

Finally, the complexities of material systems and manufacturing environments not only present challenges but also cre-

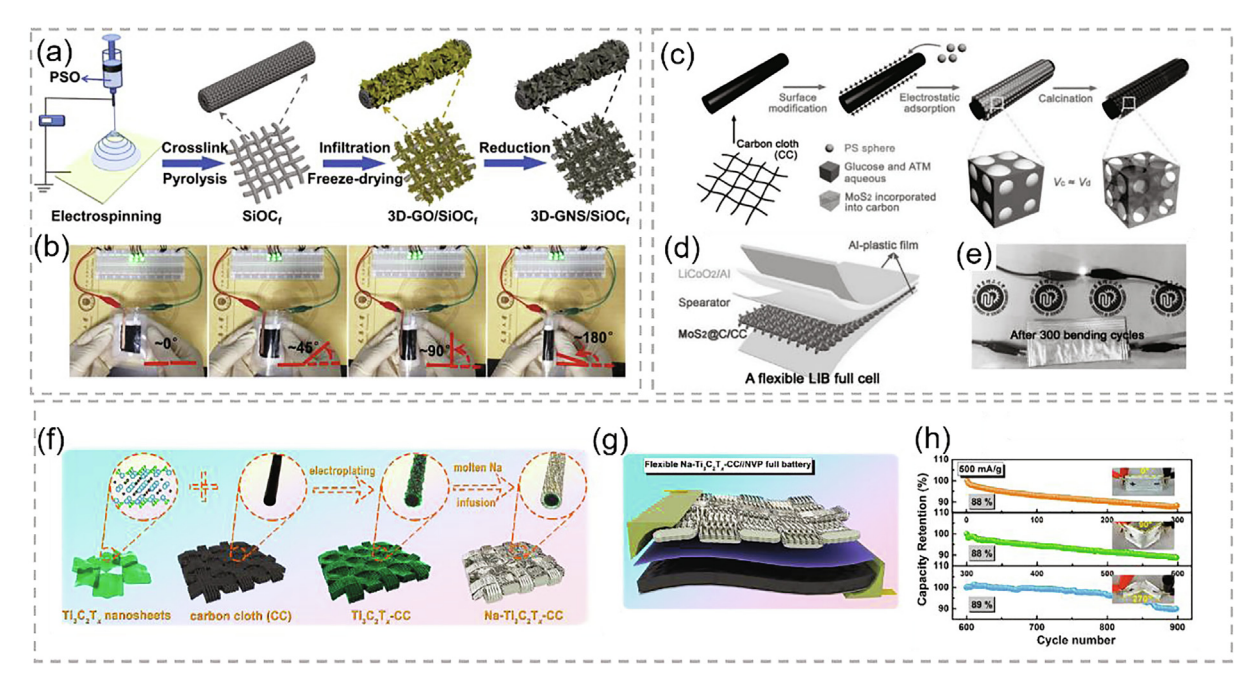


Fig. 10. The flexible stability measurement of 2DM-WBs. (a) Schematic illustration of the construction of 3D-GNS/SiOC_f cloth. (b) Optical images of the flexible cell assembled with 6 LEDs at various bending states [175]. (c) Schematic of the preparation of MoS₂@C/CC flexible electrode. (d) Schematic illustration of a flexible full battery. (e) LED powered by the flexible full battery after 300 bending cycles [177]. (f) Schematic diagram of the fabrication procedure for Ti₃C₂T_x-CC skeletons and Na-Ti₃C₂T_x-CC metal anodes. (g) Schematic structure of flexible Na-Ti₃C₂T_x-CC//NVP metal batteries. (h) Capacitance retention of Na-Ti₃C₂T_x-CC//NVP battery at different bending angles [176].

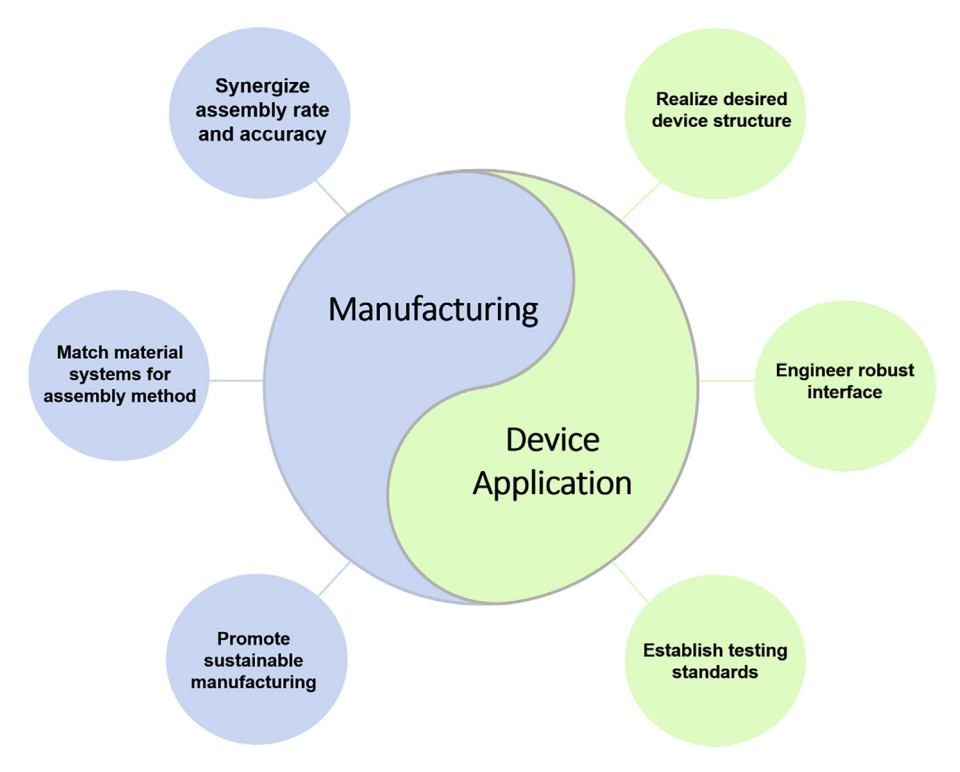


Fig. 11. Conclusions and perspectives of solution assembly of 2D materials for wearable energy storage applications.

ate unlimited opportunities to design 2DM-WESDs. It will be difficult to examine all factors experimentally. Therefore, simulation, machine learning, and data mining represent new driving forces to provide prediction, guidance, and validation. 2DM-WESDs is a highly interdisciplinary research area covering a wide span of disciplines including materials, mechanics, physics, chemistry/chemical engineering, electronics, and biology. A close collaboration and synergy of expertise across different

disciplines are desirable to promote deeper understanding and future development.

Declaration of Competing Interest

The authors declare that they have no known competing financial interests or personal relationships that could have appeared to influence the work reported in this paper.

Acknowledgments

This material is based upon work supported by the National Science Foundation, United States, NSF # 2003077, Villanova University, United States, Villanova startup fund.

References

- [1] Y. Liang, C. Zhao, H. Yuan, Y. Chen, W. Zhang, J. Huang, D. Yu, Y. Liu, M. Titirici, Y. Chueh, InfoMat 1 (2019) 6-32.
- S. Varma, K. Sambath Kumar, S. Seal, S. Rajaraman, J. Thomas, Adv. Sci. 5 [2] (2018) 1800340.
- [3] J. Di, X. Zhang, Z. Yong, Y. Zhang, D. Li, R. Li, Q. Li, Adv. Mater. 28 (2016) 10529–10538.
- [4] J. Kim, A. Campbell, B. de Ávila, J. Wang, Nat. Biotechnol. 37 (2019) 389-406.
- [5] M. Choi, J. Yang, T. Hyeon, D. Kim, npj Flexible Electronics 2 (2018) 10.
- [6] T. Schroeder, A. Guha, A. Lamoureux, G. VanRenterghem, D. Sept, M. Shtein, J. Yang, M. Mayer, Nature 552 (2017) 214–218.
- [7] H. Sun, Y. Zhang, J. Zhang, X. Sun, H. Peng, Nat. Rev. Mater. 2 (2017) 17023. [8] Z. Wen, M. Yeh, H. Guo, J. Wang, Y. Zi, W. Xu, J. Deng, L. Zhu, X. Wang, C. Hu, Sci. Adv. 2 (2016) e1600097.
- [9] C. Núñez, L. Manjakkal, R. Dahiya, npj Flexible Electronics 3 (2019) 1.
- [10] B. An, J. Shin, S. Kim, J. Kim, S. Ji, J. Park, Y. Lee, J. Jang, Y. Park, E. Cho, Polymers 9 (2017) 303.
- [11] Q. Zhang, Z. Zhou, Z. Pan, J. Sun, B. He, Q. Li, T. Zhang, J. Zhao, L. Tang, Z. Zhang, Adv. Sci. 5 (2018) 1801462.
- S. Gong, W. Cheng, Adv. Energy Mater. 7 (2017) 1700648.
- [13] P. Zhang, F. Wang, M. Yu, X. Zhuang, X. Feng, Chem. Soc. Rev. 47 (2018) 7426-7451
- [14] F. Yi, H. Ren, J. Shan, X. Sun, D. Wei, Z. Liu, Chem. Soc. Rev. 47 (2018) 3152-3188.
- [15] Y. Dong, Z. Wu, W. Ren, H. Cheng, X. Bao, Sci. Bull. 62 (2017) 724-740.
- [16] J. Pang, R. Mendes, A. Bachmatiuk, L. Zhao, H. Ta, T. Gemming, H. Liu, Z. Liu, M. Rummeli, Chem. Soc. Rev. 48 (2019) 72-133.
- B. Anasori, M. Lukatskaya, Y. Gogotsi, Nat. Rev. Mater. 2 (2017) 16098.
- [18] C. Tan, X. Cao, X. Wu, Q. He, J. Yang, Chem. Rev. 117 (2017) 6225-6331.
- [19] M. Hu, H. Zhang, T. Hu, B. Fan, X. Wang, Z. Li, Chem. Soc. Rev. 49 (2020) 6666-6693.
- [20] H. Yin, Z. Tang, Chem. Soc. Rev. 45 (2016) 4873–4891.
- X. Li, M. Sun, C. Shan, Q. Chen, X. Wei, Adv. Mater. Interfaces 5 (2018) [21] 1701246.
- [22] Y. Chen, K. Yang, B. Jiang, J. Li, M. Zeng, L. Fu, J. Mater. Chem. A 5 (2017) 8187-8208.
- X. Song, N. Li, H. Zhang, L. Wang, Y. Yan, H. Wang, L. Wang, Z. Bian, ACS Appl. [23] Mater. Interfaces 12 (2020) 17519-17527.
- X. Li, L. Zhi, Chem. Soc. Rev. 47 (2018) 3189-3216.
- J. Duan, Y. Li, Y. Pan, N. Behera, W. Jin, Coord. Chem. Rev. 395 (2019) 25-45.
- J. Zhu, E. Ha, G. Zhao, Y. Zhou, D. Huang, G. Yue, L. Hu, N. Sun, Y. Wang, L. Lee, Coord. Chem. Rev. 352 (2017) 306-327.
- [27] Y. Wu, Y. Yu, Energy Storage Mater. 16 (2019) 323-343.
- [28] X. Zhang, L. Hou, A. Ciesielski, P. Samorì, Adv. Energy Mater. 6 (2016) 1600671.
- [29] H. Guo, Z. Hu, Z. Liu, J. Tian, Adv. Funct. Mater. 31 (2021) 2007810.
- [30] T. Li, G. Li, L. Li, L. Liu, Y. Xu, H. Ding, T. Zhang, ACS Appl. Mater. Interfaces 8 (2016) 2562-2572.
- X. Cai, Y. Luo, B. Liu, H. Cheng, Chem. Soc. Rev. 47 (2018) 6224-6266.
- [32] P. Xiong, R. Ma, N. Sakai, L. Nurdiwijayanto, T. Sasaki, ACS Energy Lett. 3 (2018) 997-1005.
- [33] P. Li, Y. Maeda, Q. Xu, Chem. Commun. 47 (2011) 8436–8438.
- K. Novoselov, A. Geim, S. Morozov, D. Jiang, Y. Zhang, S. Dubonos, I. Grigorieva, A. Firsov, Science 306 (2004) 666-669.
- [35] D. Hecht, L. Hu, G. Irvin, Adv. Mater. 23 (2011) 1482-1513.
- [36] Y. Hernandez, V. Nicolosi, M. Lotya, F. Blighe, Z. Sun, S. De, I. McGovern, B. Holland, M. Byrne, Y. Gun'Ko, Nat. Nanotechnol. 3 (2008) 563-568.
- [37] C. Backes, T. Higgins, A. Kelly, C. Boland, A. Harvey, D. Hanlon, J. Coleman, Chem. Mater. 29 (2017) 243-255. [38] H. Liu, L. Liu, M. Yi, Z. Shen, S. Liang, X. Zhang, S. Ma, Chem. Eng. J. 311 (2017)
- 293-301.
- [39] W. Zhao, M. Fang, F. Wu, H. Wu, L. Wang, G. Chen, J. Mater. Chem. 20 (2010) 5817-5819.
- [40] C. Zhang, J. Tan, Y. Pan, X. Cai, X. Zou, H. Cheng, B. Liu, Natl. Sci. Rev. 7 (2020) 324-332.
- S. Yousef, A. Mohamed, M. Tatariants, Tribol. Int. 121 (2018) 54-63.
- [42] E. Varrla, K. Paton, C. Backes, A. Harvey, R. Smith, J. McCauley, J. Coleman, Nanoscale 6 (2014) 11810-11819..
- F. Bonaccorso, A. Bartolotta, J. Coleman, C. Backes, Adv. Mater. 28 (2016)
- [44] E. Nguyen, B. Carey, T. Daeneke, J. Ou, K. Latham, S. Zhuiykov, K. Kalantarzadeh, Chem. Mater. 27 (2015) 53-59.
- [45] P. Lin, J. Wu, W. Liu, Sci. Rep. 8 (2018) 9766.
- [46] A. Castillo, V. Pellegrini, A. Ansaldo, F. Ricciardella, H. Sun, L. Marasco, J. Buha, Z. Dang, L. Gagliani, E. Lago, Mater. Horiz. 5 (2018) 890-904.
- [47] R. Muzyka, M. Kwoka, Ł. Smędowski, N. Díez, G. Gryglewicz, New Carbon Mater. 32 (2017) 15-20.

- [48] W.R. Hummers Jr., Offeman J. Am. Chem. Soc. 80 (1958) 1339.
- [49] C. Li, X. Chen, L. Shen, N. Bao, ACS Omega 5 (2020) 3397-3404.
- [50] A. Zandiatashbar, G. Lee, S. An, S. Lee, N. Mathew, M. Terrones, T. Hayashi, C. Picu, J. Hone, N. Koratkar, Nat. Commun. 5 (2014) 3186.
- [51] S. Natarajan, S. Ede, H. Bajaj, S. Kundu, Colloids Surf. A Physicochem. Eng. Asp. 543 (2018) 98-108.
- [52] T. Wei, M. Zhang, P. Wu, Y. Tang, S. Li, F. Shen, X. Wang, X. Zhou, Y. Lan, Nano Energy 34 (2017) 205-214.
- [53] Q. Huang, X. Li, M. Sun, L. Zhang, C. Song, L. Zhu, P. Chen, Z. Xu, W. Wang, X. Bai, Adv. Mater. Interfaces 4 (2017) 1700171.
- [54] Y. Yin, J. Han, Y. Zhang, X. Zhang, P. Xu, Q. Yuan, L. Samad, X. Wang, Y. Wang, Z. Zhang, J. Am. Chem. Soc. 138 (2016) 7965-7972.
- [55] Z. Zeng, Z. Yin, X. Huang, H. Li, Q. He, G. Lu, F. Boey, H. Zhang, Angew. Chem. 123 (2011) 11289-11293.
- [56] M. Naguib, M. Kurtoglu, V. Presser, J. Lu, J. Niu, M. Heon, L. Hultman, Y. Gogotsi, M.W. Barsoum, Adv. Mater. 23 (2011) 4248-4253.
- [57] J. Xiao, J. Wen, J. Zhao, X. Ma, H. Gao, X. Zhang, Electrochim. Acta 337 (2020) 135803.
- [58] B. Anasori, Û. Gogotsi, Springer (2019)..
- [59] S. Kajiyama, L. Szabova, H. linuma, A. Sugahara, K. Gotoh, K. Sodeyama, Y. Tateyama, M. Okubo, A. Yamada, Adv. Energy Mater. 7 (2017) 1601873.
- [60] T. Yang, T. Song, M. Callsen, J. Zhou, J. Chai, Y. Feng, S. Wang, M. Yang, Adv. Mater. Interfaces 6 (2019) 1801160.
- [61] N. Mao, C. Zhou, D. Tong, W. Yu, C. Lin, Appl. Clay Sci. 144 (2017) 60-78.
- [62] J. ten Elshof, Y. Wang, Small Methods 3 (2019) 1800318.
- [63] M. Honda, Y. Oaki, H. Imai, Chem. Mater. 26 (2014) 3579-3585.
- [64] M. Honda, Y. Oaki, H. Imai, Chem. Commun. 51 (2015) 10046-10049.
- [65] J. Lee, B. Kang, Y. Jo, S. Hwang, ACS Appl. Mater. Interfaces 11 (2019) 12121-
- [66] A. Jawaid, D. Nepal, K. Park, M. Jespersen, A. Qualley, P. Mirau, L. Drummy, R. Vaia, Chem. Mater. 28 (2016) 337-348.
- [67] Y. Lin, B. Adilbekova, Y. Firdaus, E. Yengel, H. Faber, M. Sajjad, X. Zheng, E. Yarali, A. Seitkhan, O. Bakr, Adv. Mater. 31 (2019) 1902965.
- [68] Y. Liao, Q. Ma, Y. Shan, J. Liang, X. Dai, Y. Xiang, J. Alloys Compd. 806 (2019) 999-1007
- [69] K. Kalantar-Zadeh, J. Tang, M. Wang, K. Wang, A. Shailos, K. Galatsis, R. Kojima, V. Strong, A. Lech, W. Wlodarski, Nanoscale 2 (2010) 429-433.
- [70] A. Etman, L. Wang, K. Edström, L. Nyholm, J. Sun, Adv. Funct. Mater. 29 (2019) 1806699.
- [71] X. Rui, Z. Lu, H. Yu, D. Yang, H. Hng, T. Lim, Q. Yan, Nanoscale 5 (2013) 556-
- [72] C. Wang, Y. Yi, H. Li, P. Wu, M. Li, W. Jiang, Z. Chen, H. Li, W. Zhu, S. Dai, Nano Energy 67 (2020) 104253.
- [73] J. Foster, S. Henke, A. Schneemann, R. Fischer, A. Cheetham, Chem. Commun. 52 (2016) 10474–10477.
- [74] D. Liu, B. Liu, C. Wang, W. Jin, Q. Zha, G. Shi, D. Wang, X. Sang, C. Ni, A.C.S. Sustain, Chem. Eng. 8 (2020) 2167-2175.
- [75] U. Khan, A. O'Neill, H. Porwal, P. May, K. Nawaz, J. Coleman, Carbon 50 (2012) 470-475.
- [76] L. Zhu, J. Lang, D. Zhou, Q. Wu, B. Li, Langmuir 36 (2020) 5608-5617.
- [77] A. Lefebvre, V. McDonell, CRC press (2017)...
- [78] X. Zhang, D. Li, K. Liu, J. Tong, X. Yi, Int. J. Lightweight Mater. Manuf. 2 (2019) 241-249.
- [79] T. Tung, J. Yoo, F. Alotaibi, M. Nine, R. Karunagaran, M. Krebsz, G. Nguyen, D. Tran, J. Feller, D. Losic, ACS Appl. Mater. Interfaces 8 (2016) 16521–16532.
- [80] A. Kelly, D. Finn, A. Harvey, T. Hallam, J. Coleman, Appl. Phys. Lett. 109 (2016) 023107.
- [81] Z. Xiong, X. Yun, L. Qiu, Y. Sun, B. Tang, Z. He, J. Xiao, D. Chung, T. Ng, H. Yan, Adv. Mater. 31 (2019) 1804434.
- [82] X. Jiang, W. Li, T. Hai, R. Yue, Z. Chen, C. Lao, Y. Ge, G. Xie, Q. Wen, H. Zhang, NPJ 2D Mater. Appl. 3 (2019) 34.
- [83] A. Kelly, T. Hallam, C. Backes, A. Harvey, A. Esmaeily, I. Godwin, J. Coelho, V. Nicolosi, J. Lauth, A. Kulkarni, Science 356 (2017) 69–73.
 [84] L. Yu, W. Li, C. Wei, Q. Yang, Y. Shao, J. Sun, Nano-Micro Lett. 12 (2020) 143.
- [85] T. Tran, N. Dutta, N. Choudhury, Adv. Colloid Interface Sci. 261 (2018) 41–61.
- [86] J. Orangi, F. Hamade, V. Davis, M. Beidaghi, ACS Nano 14 (2019) 640–650.
 [87] C. Zhang, L. McKeon, M. Kremer, S. Park, O. Ronan, A. Seral-Ascaso, S. Barwich, C. Coileáin, N. McEvoy, H. Nerl, Nat. Commun. 10 (2019) 1795.
- [88] X. Huang, Y. Liu, S. Hwang, S. Kang, D. Patnaik, J. Cortes, J. Rogers, Adv. Mater. 26 (2014) 7371-7377.
- [89] Y. Aleeva, B. Pignataro, J. Mater. Chem. C 2 (2014) 6436-6453.
- [90] R. Søndergaard, M. Hösel, D. Angmo, T. Larsen-Olsen, F. Krebs, Mater. Today 15 (2012) 36-49.
- [91] P. He, J. Cao, H. Ding, C. Liu, J. Neilson, Z. Li, I. Kinloch, B. Derby, A.C.S. Appl, Mater. Interfaces 11 (2019) 32225–32234.
 [92] J. Qu, N. He, S. Patil, Y. Wang, D. Banerjee, W. Gao, ACS Appl. Mater. Interfaces
- 11 (2019) 14944-14951. [93] S. Abdolhosseinzadeh, R. Schneider, A. Verma, J. Heier, F. Nüesch, C. Zhang,
- Adv. Mater. 32 (2020) 2000716. [94] L. Ng, X. Zhu, G. Hu, N. Macadam, D. Um, T. Wu, F. Le Moal, C. Jones, T. Hasan,
- Adv. Funct. Mater. 29 (2019) 1807933. [95] W. Hyun, E. Secor, M. Hersam, C. Frisbie, L. Francis, Adv. Mater. 27 (2015) 109-115
- [96] A. Berni, M. Mennig, H. Schmidt, Springer, (2004) 89-92...
- N. Stepina, M. Galkov, M. Predtechenskiy, A. Bezrodny, V. Kirienko, A. Dvurechenskii, Modern Electron. Mater. 5 (2019) 21.

- 1981 G. Grau, R. Kitsomboonloha, V. Subramanian, 9568 Int. Soc. Opt. Photonics (2015) 95680M..
- [99] Q. Zhang, L. Huang, Q. Chang, W. Shi, L. Shen, Q. Chen, Nanotechnology 27 (2016) 105401.
- [100] H. Li, Z. Song, X. Zhang, Y. Huang, S. Li, Y. Mao, H. Ploehn, Y. Bao, M. Yu, Science 342 (2013) 95-98.
- [101] J. Wang, B. Liu, Sci. Technol. Adv. Mater. 20 (2019) 992-1009.
- [102] Z. Weng, Y. Su, D. Wang, F. Li, J. Du, H. Cheng, Adv. Energy Mater. 1 (2011) 917-922.
- [103] C. Lim, D. Min, S. Lee, Appl. Phys. Lett. 91 (2007) 243117.
- [104] L. Paliotta, G. De Bellis, A. Tamburrano, F. Marra, A. Rinaldi, S. Balijepalli, S. Kaciulis, M. Sarto, Carbon 89 (2015) 260-271.
- [105] Q. Zou, W. Guo, L. Zhang, L. Yang, Z. Zhao, F. Liu, X. Ye, Y. Zhang, W. Shi, Nanotechnology 50 (2020) 505710.
- [106] H. Huang, J. He, Z. Wang, H. Zhang, L. Jin, N. Chen, Y. Xie, X. Chu, B. Gu, W. Deng, Nano Energy 69 (2020) 104431.
- [107] Y. Huang, K. Chou, Ceram. Int. 29 (2003) 485-493.
- [108] G. Weng, J. Li, M. Alhabeb, C. Karpovich, H. Wang, J. Lipton, K. Maleski, J. Kong, E. Shaulsky, M. Elimelech, Adv. Funct. Mater. 28 (2018) 1803360.
- [109] K. Ariga, Langmuir 36 (2020) 7158-7180.
- [110] G. Wang, H. Qin, X. Gao, Y. Cao, W. Wang, F. Wang, H. Wu, H. Cong, S. Yu, Chem 4 (2018) 896-910.
- [111] D. Petukhov, A. Chumakov, A. Kan, V. Lebedev, A. Eliseev, O. Konovalov, A. Eliseev, Nanoscale 11 (2019) 9980-9986.
- [112] M. Parchine, J. McGrath, M. Bardosova, M. Pemble, Langmuir 32 (2016) 5862-
- [113] L. Xu, A. Tetreault, H. Khaligh, I. Goldthorpe, S. Wettig, M. Pope, Langmuir 35 (2018) 51-59.
- [114] J. Puetz, M. Aegerter, Springer (2004) 37-48.
- [115] D. Grosso, J. Mater. Chem. 21 (2011) 17033-17038.
- [116] G. Barroso, Q. Li, R. Bordia, G. Motz, J. Mater. Chem. A 7 (2019) 1936–1963.
- [117] M. Aegerter, J. Puetz, G. Gasparro, N. Al-Dahoudi, Opt. Mater. 26 (2004) 155-
- [118] B. Li, H. Jung, H. Wang, Y. Kim, T. Kim, M. Hahm, A. Busnaina, M. Upmanyu, Y. Jung, Adv. Funct. Mater. 21 (2011) 1810-1815.
- [119] M. Nordlund, S. Bhandary, B. Sanyal, N. Almqvist, T. Löfqvist, H. Grennberg, J. Phys. D Appl. Phys. 49 (2016) 07LT01.
- [120] A. Levitt, D. Hegh, P. Phillips, S. Uzun, M. Anayee, J. Razal, Y. Gogotsi, G. Dion, Mater. Today 34 (2020) 17-29.
- [121] S. Su, L. Lai, R. Li, Y. Lin, H. Dai, X. Zhu, ACS Appl. Energy Mater. 3 (2020) 9379-9389.
- [122] D. Zhou, J. Hao, A. Clark, K. Kim, L. Zhu, J. Liu, X. Cheng, B. Li, A.C.S. Appl, Mater. Interfaces 11 (2019) 33458-33464.
- [123] A. Ozcelik, J. Rufo, F. Guo, Y. Gu, P. Li, J. Lata, T. Huang, Nat. Methods 15 (2018) 1021-1028.
- [124] Z. Mao, Y. Xie, F. Guo, L. Ren, P. Huang, Y. Chen, J. Rufo, F. Costanzo, T. Huang, Lab Chip 16 (2016) 515-524.
- [125] I. Perelshtein, G. Applerot, N. Perkas, J. Grinblat, E. Hulla, E. Wehrschuetz-Sigl, A. Hasmann, G. Guebitz, A. Gedanken, ACS Appl. Mater. Interfaces 2 (2010) 1999-2004.
- [126] D. Zhou, M. Han, B. Sidnawi, Q. Wu, Y. Gogotsi, B. Li, Appl. Mater. Today 22 (2021) 100956.
- [127] C. Couly, M. Alhabeb, K. Van Aken, N. Kurra, L. Gomes, A. Navarro-Suárez, B. Anasori, H. Alshareef, Y. Gogotsi, Adv. Electron. Mater. 4 (2018) 1700339.
- [128] W. Xie, Y. Wang, J. Zhou, M. Zhang, J. Yu, C. Zhu, J. Xu, Appl. Surf. Sci. 534 (2020) 147584.
- [129] E. Miller, Y. Hua, F. Tezel, J. Energy Storage 20 (2018) 30-40.
- [130] K. Li, X. Liu, S. Chen, W. Pan, J. Zhang, J. Energy Chem. 32 (2019) 166–173.
- [131] K. Li, Y. Huang, J. Liu, M. Sarfraz, P. Agboola, I. Shakir, Y. Xu, J. Mater. Chem. A 6 (2018) 1802-1808
- [132] J. Li, Q. Shi, Y. Shao, C. Hou, Y. Li, Q. Zhang, H. Wang, Energy Storage Mater. 16 2019) 212-219.
- [133] H. Jiang, Z. Wang, Q. Yang, M. Hanif, Z. Wang, L. Dong, M. Dong, Electrochim. Acta 290 (2018) 695–703.
- [134] W. Shao, M. Tebyetekerwa, I. Marriam, W. Li, Y. Wu, S. Peng, S. Ramakrishna,
- S. Yang, M. Zhu, J. Power Sour. 396 (2018) 683-690. [135] M. Wang, H. Shi, P. Zhang, Z. Liao, M. Wang, H. Zhong, F. Schwotzer, A. Nia, E.
- Zschech, S. Zhou, Adv. Funct. Mater. 30 (2020) 2002664. [136] H. Xiao, Z. Wu, L. Chen, F. Zhou, S. Zheng, W. Ren, H. Cheng, X. Bao, ACS Nano 11 (2017) 7284-7292.
- [137] M. Lukatskaya, S. Kota, Z. Lin, M. Zhao, N. Shpigel, M. Levi, J. Halim, P. Taberna, M. Barsoum, P. Simon, Nat. Energy 2 (2017) 17105.
- [138] C. Lee, X. Wei, J. Kysar, J. Hone, Science 321 (2008) 385-388.
- [139] J. Come, Y. Xie, M. Naguib, S. Jesse, S. Kalinin, Y. Gogotsi, P. Kent, N. Balke, Adv. Energy Mater. 6 (2016) 1502290.
- [140] S. Dutta, S. Pal, S. De, New J. Chem. 43 (2019) 12385–12395.
- [141] Q. Chang, L. Li, L. Sai, W. Shi, L. Huang, Adv. Electron. Mater. 4 (2018) 1800059.

- [142] W. Hyun, E. Secor, C. Kim, M. Hersam, L. Francis, C. Frisbie, Adv. Energy Mater. 7 (2017) 1700285.
- [143] T. An, W. Cheng, J. Mater. Chem. A 6 (2018) 15478-15494.
- [144] I. Moon, B. Ki, J. Oh, Chem. Eng. J. 392 (2020) 123794.
- [145] T. Chang, T. Zhang, H. Yang, K. Li, Y. Tian, J. Lee, P. Chen, ACS Nano 12 (2018) 8048-8059.
- [146] S. Zheng, X. Tang, Z. Wu, Y. Tan, S. Wang, C. Sun, H. Cheng, X. Bao, ACS Nano 11 (2017) 2171-2179.
- [147] Y. Zhong, X. Zhang, Y. He, H. Peng, G. Wang, G. Xin, Adv. Funct. Mater. 28 (2018) 1801998.
- [148] S. Uzun, S. Seyedin, A. Stoltzfus, A. Levitt, M. Alhabeb, M. Anayee, C. Strobel, J. Razal, G. Dion, Y. Gogotsi, Adv. Funct. Mater. 29 (2019) 1905015.
- [149] H. Zhou, Y. Lu, F. Wu, L. Fang, H. Luo, Y. Zhang, M. Zhou, J. Alloys Compd. 802 (2019) 259-268.
- [150] X. Wang, H. Li, H. Li, S. Lin, W. Ding, X. Zhu, Z. Sheng, H. Wang, X. Zhu, Y. Sun, Adv. Funct. Mater. 30 (2020) 0190302.
- [151] M. Hu, T. Hu, R. Cheng, J. Yang, C. Cui, C. Zhang, X. Wang, J. Energy Chem. 27 (2018) 161-166. [152] C. Zhang, M. Kremer, A. Seral-Ascaso, S. Park, N. McEvoy, B. Anasori, Y.
- Gogotsi, V. Nicolosi, Adv. Funct. Mater. 28 (2018) 1705506. [153] L. Yu, Z. Fan, Y. Shao, Z. Tian, J. Sun, Z. Liu, Adv. Energy Mater. 9 (2019)
- 1901839.
- [154] Z. Zhou, W. Panatdasirisuk, T. Mathis, B. Anasori, C. Lu, X. Zhang, Z. Liao, Y. Gogotsi, S. Yang, Nanoscale 10 (2018) 6005-6013.
- [155] Y. Zhou, K. Maleski, B. Anasori, J. Thostenson, Y. Pang, Y. Feng, K. Zeng, C. Parker, S. Zauscher, Y. Gogotsi, ACS Nano 14 (2020) 3576-3586.
- [156] K. Wang, B. Zheng, M. Mackinder, N. Baule, H. Qiao, H. Jin, T. Schuelke, Q. Fan, Energy Storage Mater. 20 (2019) 299-306.
- [157] D. Tripkovic, Nature 5 (2020) 259-270.
- [158] Z. Zhou, W. Si, P. Lu, W. Guo, L. Wang, T. Zhang, F. Hou, J. Liang, J. Energy Chem. 47 (2020) 29-37.
- [159] W. Guo, X. Yan, F. Hou, L. Wen, Y. Dai, D. Yang, X. Jiang, J. Liu, J. Liang, S. Dou, Carbon 152 (2019) 888-897.
- [160] W. Guo, W. Si, T. Zhang, Y. Han, L. Wang, Z. Zhou, P. Lu, F. Hou, J. Liang, J. Energy Chem. 54 (2021) 746-753.
- I. Son, J. Park, S. Kwon, S. Park, M. Rümmeli, A. Bachmatiuk, H. Song, J. Ku, J. Choi, J. Choi, Nat. Commun. 6 (2015) 7393.
- [162] L. Wang, Q. Zhang, J. Zhu, X. Duan, Z. Xu, Y. Liu, H. Yang, B. Lu, Energy Storage Mater. 16 (2019) 37-45.
- [163] M. Okubo, A. Sugahara, S. Kajiyama, A. Yamada, Acc. Chem. Res. 51 (2018) 591-599.
- [164] Z. Jiang, T. Liu, L. Yan, J. Liu, F. Dong, M. Ling, C. Liang, Z. Lin, Energy Storage Mater. 11 (2018) 267–273.
- [165] Z. Sang, X. Yan, D. Su, H. Ji, S. Wang, S. Dou, J. Liang, Small 16 (2020) 2001265.
- [166] P. Lu, X. Wang, L. Wen, X. Jiang, W. Guo, L. Wang, X. Yan, F. Hou, J. Liang, H. Cheng, Small 15 (2019) 1805064.
- [167] X. Tang, D. Zhou, P. Li, X. Guo, C. Wang, F. Kang, B. Li, G. Wang, ACS Cent. Sci. 5 (2019) 365-373.
- [168] S. Zheng, Z. Wu, F. Zhou, X. Wang, J. Ma, C. Liu, Y. He, X. Bao, Nano Energy 51 (2018) 613–620.
- [169] M. Bai, K. Xie, K. Yuan, K. Zhang, N. Li, C. Shen, Y. Lai, R. Vajtai, P. Ajayan, B. Wei, Adv. Mater. 30 (2018) 1801213. [170] H. Shi, M. Yue, C. Zhang, Y. Dong, P. Lu, S. Zheng, H. Huang, J. Chen, P. Wen, Z.
- Xu, ACS Nano 14 (2020) 8678-8688. [171] C. Zhang, S. Park, A. Seral-Ascaso, S. Barwich, N. McEvoy, C. Boland, J.
- Coleman, Y. Gogotsi, V. Nicolosi, Nat. Commun. 10 (2019) 849.
- [172] K. Shen, B. Li, S. Yang, Energy Storage Mater. 24 (2020) 670-675.
- [173] Z. Fang, N. Ma, K. Zhang, K. Xie, C. Shen, J. Peng, Y. Dang, W. Cheng, D. Zheng, L. Li, Ionics 25 (2019) 3099-3106.
- [174] J. Janek, W. Zeier, Nat. Energy 1 (2016) 16141.
 [175] Z. Sang, X. Yan, L. Wen, D. Su, Z. Zhao, Y. Liu, H. Ji, J. Liang, S. Dou, Energy Storage Mater. 25 (2020) 876-884.
- [176] Y. Fang, R. Lian, H. Li, Y. Zhang, Z. Gong, K. Zhu, K. Ye, J. Yan, G. Wang, Y. Gao, ACS Nano 14 (2020) 8744-8753.
- [177] Z. Deng, H. Jiang, Y. Hu, Y. Liu, L. Zhang, H. Liu, C. Li, Adv. Mater. 29 (2017) 1603020.
- [178] Y. Zhao, X. Yang, L. Kuo, P. Kaghazchi, Q. Sun, J. Liang, B. Wang, A. Lushington, R. Li, H. Zhang, Small 14 (2018) 1703717. [179] N. Aliahmad, Y. Liu, J. Xie, M. Agarwal, ACS Appl. Mater. Interfaces 10 (2018)
- 16490-16499.
- [180] H. Tao, L. Xiong, S. Zhu, X. Yang, L. Zhang, Int. J. Hydrogen Energy 41 (2016) 21268-21277. [181] K. Fu, Y. Wang, C. Yan, Y. Yao, Y. Chen, J. Dai, S. Lacey, Y. Wang, J. Wan, T. Li,
- Adv. Mater. 28 (2016) 2587-2594. [182] J. Gu, Q. Zhu, Y. Shi, H. Chen, D. Zhang, Z. Du, S. Yang, ACS Nano 14 (2020) 891_898
- [183] A. Benítez, J. Amaro-Gahete, D. Esquivel, F. Romero-Salguero, J. Morales, Á. Caballero, Nanomaterials 10 (2020) 424.